Title
Variable Daily Autocorrelation Functions of High-Frequency Seismic Data on Mars

Journal
Seismological Research Letters, 94(2A)

ISSN
0895-0695

Authors
Qin, Lei
Qiu, Hongrui
Nakata, Nori
et al.

Publication Date
2023-03-01

DOI
10.1785/0220220196

Variable daily autocorrelation functions of high frequency seismic data on Mars

Lei Qin[1,2], Hongrui Qiu[2*], Nori Nakata[2], Sizhuang Deng[3], Alan Levander[3], Yehuda Ben-Zion[4,5]

[1]Institute of Geophysics and Geomatics, China University of Geosciences, Wuhan, China

[2]Earth, Atmospheric and Planetary Sciences, Massachusetts Institute of Technology, Cambridge, MA, USA

[3]Department of Earth, Environmental and Planetary Sciences, Rice University, Houston, TX, USA

[4]Department of Earth Sciences, University of Southern California, Los Angeles, CA, USA

[5]Southern California Earthquake Center, University of Southern California, Los Angeles, CA, USA

*Corresponding author: Hongrui Qiu (qiuhonrui@gmail.com)

Declaration of Competing Interests: The authors acknowledge there are no conflicts of interest recorded.

Abstract

High frequency seismic data on Mars are dominated by wind-generated lander vibrations, which are radiated partially to the subsurface. Autocorrelation functions (ACFs) of seismic data on Mars filtered between 1-5 Hz show clear phases at ~1.3 sec, ~2.6 sec, and ~3.9 sec. Daily temporal changes of their arrival times (*dt/t*) correlate well with the daily changes of ground temperature, with ~5% daily variation and ~50-min apparent phase delay. The following two mechanisms could explain the observations: (1) the interference of two predominant spectral peaks at ~3.3 Hz and ~4.1 Hz, assumed to be both lander resonance modes, generate the apparent arrivals in the ACFs; (2) the interference of the lander vibration and its reflection from an interface ~200 m below the lander, generate the 3.3 Hz spectral peak and ~1.3 sec arrival in the ACFs. The driving mechanism of the resolved *dt/t* that most likely explains the ~50-min delay is thermoelastic strain at a near-surface layer, affecting the lander-ground coupling and subsurface structures. The two outlined mechanisms suggest, respectively, up to ~10% changes in ground stiffness at 1-5 Hz and ~15% velocity changes in the top ~20 m layer. These are upper bound values considering also other possible contributions. The presented methodology and results contribute to analysis of ACFs with limited data and the understanding of subsurface materials on Mars.

Keywords: seismic interferometry; temporal velocity changes, source effects; subsurface structural effects; thermoelastic strain

Introduction

Seismic interferometry is widely used to image and monitor seismic structures and buildings on Earth (Shapiro & Campillo 2004, Lin *et al.* 2013, Phạm & Tkalčić 2017, Romero & Schimmel 2018). Velocity variations are observed in relation to earthquakes (Peng & Ben-Zion 2006, Karabulut & Bouchon 2007, Prieto *et al.* 2010, Froment *et al.* 2013, Qin *et al.* 2020), volcanic activity (Brenguier *et al.* 2008), and periodic (e.g., daily, seasonal) environmental loadings such as hydrological changes, thermoelastic strain and tides (Ben-Zion & Allam 2013, Johnson *et al.* 2017, Mao *et al.* 2019). The autocorrelation function (ACF), a form of seismic interferometry, is considered an approximation of the zero-offset reflection seismogram beneath a site (Claerbout 1968). Since it only requires a single station, ACF provides an efficient tool for imaging and monitoring temporal changes of seismic properties below the surface (Richter *et al.* 2014, Bonilla *et al.* 2019, De Plaen *et al.* 2019, Kim & Lekic 2019, Lu & Ben-Zion 2022), especially when a limited number of seismic stations are available. These studies shed light on properties and susceptibility of subsurface materials to failure, which are of great importance to interpreting observed seismic motion, reliability of underground facilities, and other applications.

On Mars, a seismic station has been deployed by NASA's Interior Exploration using the Seismic Investigations, Geodesy and Heat Transport (InSight) mission at the end of 2018 (Panning *et al.* 2017, Lognonné *et al.* 2019). This provides the first direct geophysical data to investigate the internal structure of Mars, and several studies used ACF to retrieve information on subsurface structures. Deng & Levander (2020) identified prominent body-wave reflection phases in stacked vertical component ambient noise autocorrelation data, and associated them with reflections from deep interfaces (e.g., the Martian Moho at 39 km depth and the core-mantle boundary at ~1560 km). In a higher frequency band of 1-9 Hz, Schimmel *et al.* (2021) observed potential subsurface *P*-wave reflection at ~10.6 sec using phase cross-correlation, which may indicate a ~21-km-deep Martian crust. This is partially confirmed by Knapmeyer-Endrun *et al.* (2021) based on joint analysis of receiver function and ACF in multiple frequency bands (mainly at ~1-3.5 Hz), implying that the crust of Mars is either ~20 km or ~39 km thick at the landing site. In addition to *P*-wave reflections, Suemoto *et al.* (2020) showed that *S*-waves reflected at a shallow interface with a two-way travel time of ~1.2 sec can be extracted from the ACF of diffused ambient noise data at 5-7 Hz. Compaire *et al.* (2022) used coda waves of high-frequency seismic events to monitor long-term variations in subsurface structures on Mars and found ~3% annual fluctuations in relative velocity changes (*dt/t*) that correlated with variations in some frequency bands between 5-8 Hz. They attribute the seasonal variation of *dt/t* to velocity changes in the shallow regolith layer due to thermoelastic strain.

Interpreting ACFs on Mars is challenging because the seismic waveforms include complicated transient and sustained signals that may affect the ACFs (Kim *et al.* 2021). There are strong daily variations of wind and temperature on Mars (Fig. 1) and the noise level is elevated during the daytime (Lognonné *et al.* 2020, Suemoto *et al.* 2020). Analyses of amplitude (e.g., Panning *et al.* 2020) and polarization (Suemoto *et al.* 2020) of the data suggest that the dominant noise sources above 1 Hz are ground motions associated with wind-generated lander vibrations. The continuous records contain multiple strong peaks at 1-9 Hz (Dahmen *et al.* 2021), interpreted in previous studies as resonances of wind-generated lander vibrations. Large daily variations that correlate well with the temperature variations are observed by tracking these spectral peaks (e.g., Fig. 1c). Previous studies suggested that these daily variations are produced by the expansion and contraction of the lander in response to the daily temperature changes (Kim *et al.* 2021). However, the origin of these spectral peaks and their variations may be more complicated for two reasons: (1) no modeling of lander resonance mode that directly matches the observation has been done, due to the irregular lander structure and its complicated interaction with the highly varying wind on Mars. To our best knowledge, only Murdoch *et al.* (2018) modeled the lander resonance modes using a simplified mechanical model, and concluded the resonance modes of the lander are generally larger than 10 Hz; (2) some spectral peaks may also be explained by reverberations of the lander vibrations within a shallow low-velocity layer beneath the lander (Murphy *et al.* 1971, Shearer & Orcutt 1987, Steidl *et al.* 1996). Here, we present a detailed analysis of ACFs of seismic data recorded on Mars and discuss multiple mechanisms that could explain observed features of spectral peaks, along with possible implications on subsurface properties beneath the lander.

In section Analysis Of ACFs, we compute the ACFs in 1-5 Hz, measure and curve fit the relative travel time changes (*dt/t*) of a secondary arrival at ~1.3 sec of the ACFs, and examine the relative changes of spectral peak locations (*df/f*) in ACFs at 1-10 Hz. In section Monitoring Subsurface Structures Using ACFs, we discuss mechanisms involving two hypotheses that could explain the secondary arrival in ACFs: (1) the interference of two predominant spectral peaks if the ~3.3 Hz and ~4.1 Hz spectral peaks are wind-generated lander resonance modes; (2) the summation of the local source signal (i.e. lander vibration at ~4.1 Hz) and its reflection from an interface ~200 m below the lander, which also generates the ~3.3 Hz spectral peak. A comparison between the ground temperature and observed *dt/t* suggests that the driving mechanism of the resolved temporal changes is likely thermoelastic strain at the subsurface. In section Velocity Variation Induced By Thermoelastic Strain, we model the velocity variations induced by thermoelastic strain with reasonable parameters, and demonstrate that thermoelastic strain calculated in the top ~20 m is sufficient to produce the observed amplitude and phase of the temporal changes in the ACFs. The results are discussed and summarized in section Discussion And Conclusions. The presented analyses and results complement previous seismological studies on Mars and advance the understanding of the InSight data and subsurface materials beneath the lander.

Analysis Of ACFs

Data

The InSight mission deployed short period (SP) and very broadband (VBB) sensors recording ground motion continuously on Mars with sampling rates of 100 Hz and 20 Hz, respectively. The noise floor is ~3×10^{-9} m s^{-2} Hz$^{-1/2}$ for the SP sensors and slightly above 1×10^{-10} m s^{-2} Hz$^{-1/2}$ for the VBB sensors (Banerdt *et al.* 2020). Since we focus on high-frequency seismic signals, we use the 100 Hz recordings from the SP sensors. Environmental data are also available, including wind, air temperature, and ground temperature (Fig. 1a). It is interesting to note that there is a ~2-hour phase delay between the air temperature recorded at ~1.4 m above the ground and the ground temperature (Fig. 1a) derived from the radiometer recording (Spohn *et al.* 2018). This is due to the incoming radiation from the Sun first heating up the ground, then the air temperature increasing by absorbing the outgoing longwave radiation. The ground temperature is used in our analyses to investigate possible temperature-induced changes in subsurface seismic velocities.

Fig. 1(b)-(c) show the one-day (sol 98) EW component seismic data and corresponding spectrogram, respectively. The large amplitude wave packets, e.g., between 8 am and 12 pm (Fig. 1b), are related to strong wind velocities (Fig. 1a). Multiple spectral peaks (e.g., ~3.3, ~4.1, ~6.8, ~8.5, and ~9.8 Hz) are observed with clear daily variations in amplitudes and frequencies (Fig. 1c). Amplitude (e.g., Lognonné *et al.* 2020) and polarization (Suemoto *et al.* 2020) analyses of seismic data at 1-10 Hz indicate that seismic noise sources above 1 Hz are dominated by ground motions associated with wind-generated lander vibrations.

Calculation Of ACF

The ACF is a convolution of source and zero-offset impulse response functions at the analyzed station. Here we compute and analyze ACFs of seismic recordings during sol 98 to infer characteristics of noise sources (e.g. lander vibration) and subsurface properties beneath the station.

We first divide the waveform by its smoothed envelope function (Fig. 1b) to balance the amplitude distribution in the time domain. ACFs are then computed using the continuous seismic recording in 20-sec-long moving windows with 50% overlap. For ACF analysis in the time domain, we bandpass filter the ACFs between 1-5 Hz to simplify the analysis by excluding spectral peaks at high frequencies (e.g., ~6.8, ~8.5 and ~9.8 Hz).

The ACF calculated at a specific 20-sec-long time window is illustrated as the black curve in Fig. 2(a) with its spectrum shown in Fig. 2(b). Secondary arrivals at ~1.3 sec, ~2.6 sec, and ~3.9 sec with decreasing amplitudes are seen in the ACF. However, they are not well separated from the zero-lag and each other as the ACF is dominated by signals at ~4 Hz (Fig. 2b). To improve the quality of the secondary phases, we apply spectral whitening to the ACFs by deconvolving an estimated source time function from the ACFs (Fig. 2). Since the actual source time function is unknown, we use the running average of the ACF spectrum (e.g., blue curve in Fig. 2b) with a window size of $\Delta f = 1/\Delta t_{est}$ in the spectral whitening (Oren & Nowack 2017), where $\Delta t_{est} \approx 1.3$ sec is the arrival time of the largest secondary phase in the stacked ACF. The results are almost identical using different smoothing window lengths ranging from 0.67 Hz to 1 Hz, so the deconvolution process is insensitive to the precise choice of the moving window size. To increase the signal-to-noise ratio, we stack every 30 consecutive ACFs and normalize the stacked trace by its maximum amplitude. The choice of the stacking size is made to balance the trade-off between time resolution (~5 minutes) and the quality of the resulting temporal pattern.

Temporal Changes Of ACF

Fig. 3(a) shows the ACFs computed at the EW component following the procedure described above, where daily variations in arrival times of all three secondary phases are observed. We note that the weaker phases at ~2.6 sec and ~3.9 sec are multiples of the phase at ~1.3 sec as (1) their arrival times are multiples of ~1.3 sec and (2) the relative arrival time changes (*dt/t*) are the same. Thus, we only focus on the phase at ~1.3 sec and measure its *dt/t* by approximating *t* as the arrival time in the stacked ACF envelope function (e.g., 1.36 sec in Fig. 3b). We measure *dt* values by cross correlating a target ACF with the daily stacked ACF in the time window centered on the phase (e.g., blue lines in Fig. 3b). The cross-correlation window length is given by six times the dominant period $T_c = 1/f_c$, where f_c (i.e., ~4 Hz) is estimated from the median amplitude spectrum of all ACFs. The NS and vertical components show similar results and are presented in Figs. S1-S3 (Electronic supplement).

Fig. 4(a) shows the measured *dt/t* of the secondary phase at ~1.3 sec for the EW component. The *dt/t* curve exhibits a ~5% daily variation that correlates well with the ground temperature recording with ~1-hour delay in the peak location. Therefore, we fit the *dt/t* curve with a linear transformation of the ground temperature recording $T(t)$, i.e., $g(T; a, b, t_0) = a \cdot (T(t - t_0) - b)$, where t_0 represents a delay time, a is a scaling factor, and b is a constant coefficient given by the median ground temperature during nighttime. The same data fitting can be achieved with time shifts t_0 that differ by multiples of one Martian day (T_M), so the time shift can be written as $t_d = t_0 + T_M \cdot M$, where M is an integer. Thus, we require $-T_M/2 < t_0 < T_M/2$ in the curve fitting and the resolved t_0 may be cycle-skipped. The best-fitting parameters t_0 and a are obtained via a grid search by minimizing the L_2 norm of the difference between $g(T; a, b, t_0)$ and observed *dt/t*. The best fitting t_0 is ~50 minutes (Fig. 4b). The best fitting curve $g(T; a, b, t_0)$ is depicted as the red curve in Fig. 4(a) and matches well the *dt/t* curve, especially during the Martian night and at the onset of the sharp temperature increase at ~7 am. During the daytime, the best fitting curve is slightly wider than the *dt/t* curve (i.e., steeper changes in *dt/t* at sunrise and sunset), which likely indicates nonlinear processes related to large temperature gradients during the sunrise and sunset.

Similar daily variations with a negative correlation to the ground temperature are seen in spectral peaks of ACFs, i.e., spectral peak locations decrease during daytime. Fig. 5 shows temporal changes of five spectral peak locations (i.e., ~3.3, ~4.1, ~6.8, ~8.5, and ~9.8 Hz) in EW component ACFs between 1-10 Hz. The temporal variation of a target spectral peak at frequency *f* is given by *df/f* = $(f - f_0)/f_0$, where f_0 is the median frequency of the target spectral peak during the nighttime. We also fit the observed −*df/f* curve (Fig. 5b) with a linearly scaled ground temperature following the same procedure described above. Amplitudes of the spectral peak daily variation generally increase with frequency (~5% at ~3.3 and ~4.1 Hz, ~14% at 6.8 Hz, ~21% at 8.5 Hz, and ~25% at 9.8 Hz), whereas the corresponding phase delays decrease from ~45 minutes at frequencies below 5 Hz to ~20-30 minutes for spectral peaks above 5 Hz (Fig. 5b).

Monitoring Subsurface Structures Using ACFs

The ACFs of the seismic data contain information on both the noise sources on Mars and subsurface structures beneath the lander. With known noise sources, one can deconvolve the source information from the ACF and obtain a good approximation of the zero-offset seismogram recorded at the lander. However, with the wind-generated lander vibrations as the dominant noise source on Mars (e.g., Lognonné *et al.* 2020, Suemoto *et al.* 2020), quantitative analysis of noise source properties is challenging because the lander vibrations depend on the wind strength and direction, the shape of the lander (e.g., the solar panel) and the ground properties (e.g., ground stiffness and damping), all of which are not well constrained (Murdoch *et al.* 2017, 2018, Panning *et al.* 2020).

Previous studies (e.g., Kim *et al.* 2021) concluded that all the observed spectral peaks (e.g., ~3.3, ~4.1, ~6.8, ~8.5, and ~9.8 Hz in Fig. 3a) are resonance modes of the source (i.e., lander vibration), in which case the arrival at ~1.3 sec in ACF is likely associated with the interference of source resonance modes. However, some weaker spectral peaks (e.g., at ~3.3 Hz) may also be associated with the reverberations of seismic waves in subsurface layers (e.g., Shearer & Orcutt 1987), especially considering the various velocity contrast interfaces in shallow structures on Mars (e.g., Lognonné *et al.* 2020). We therefore discuss mechanisms associated with two end-member hypotheses that could explain the observations from ACFs, related to the source properties (Hypothesis I – all spectral peaks are lander resonance modes) and subsurface structures (Hypothesis II – the spectral peak at ~3.3 Hz and perhaps others are associated with site resonance modes). As discussed in section Can We Distinguish Between The Two Hypotheses, it is difficult to distinguish between these hypotheses even with additional analysis of on-deck data, so both should be considered at present viable.

Hypothesis I – All Spectral Peaks Are Lander Resonance Modes

If all the observed spectral peaks (e.g., ~3.3, ~4.1, ~6.8, ~8.5, and ~9.8 Hz in Fig. 5a) are lander resonance modes, they may interfere with each other to produce apparent arrivals in ACFs. Specifically, the two resonance modes at ~3.3 Hz (f_1) and ~4.1 Hz (f_2) can generate oscillations in ACF at a period of $\Delta t = 1/(f_2 - f_1) \approx 1.25$ sec (e.g., Xu *et al.* 2008), consistent with the secondary arrival at ~1.3 sec in ACF. The ~5% variations and phase delays (~40-45 min) relative to the ground temperature of the 3.3 Hz and 4.1 Hz resonance modes could result in similar temporal patterns of dt/t, compatible with our observation. In this case, ACF is not a good approximation of the zero-offset reflection seismogram, and dt/t variations correspond to variations of the lander vibration at 3.3 and 4.1 Hz. The spectral peaks at higher frequencies may indicate higher modes or the vibration of different parts of the lander. Since we obtain similar results from the three components, this hypothesis also implies that the lander resonance modes in EW, NS and vertical directions are similar, generating similar interference patterns in the three-component ACFs.

Since the lander resonance modes mainly depend on the lander structure and ground stiffness affecting the lander-ground coupling (Murdoch *et al.* 2018), the resonance mode variations indicate lander structural and/or near-surface ground stiffness changes. The similarity between *df/f* and ground temperature suggests the resonance changes are induced by the temperature variations. As temperature increases, the lander material expands and the ground stiffness decreases leading to decreasing resonance modes (Murdoch *et al.* 2018). This is consistent with our observation, which in this case indicates combined effects of lander structural and ground stiffness changes.

Considering that the lander material is made of metal, it is expected to respond rapidly to the incoming solar energy and be heated by solar radiation almost simultaneously with or faster than the ground. Thus, temporal changes of the lander material (i.e. *dt/t* and *df/f*) are expected to precede, be in phase, or be only slightly delayed (e.g., a few minutes) relative to the ground temperature. However, the near-surface ground materials, mainly composed of sediments and rocks, are expected to deform by thermoelastic strain in response to the ground temperature variations with considerable phase delays. While the lander structural variations are not negligible, the considerable phase delay (~20-50 minutes) of *dt/t* and *df/f* curves relative to the ground temperature (Figs 4&5) indicate considerable contribution from ground stiffness changes.

It is difficult to quantitatively estimate the resonance frequency changes from lander structural variations because of its irregular structure and complicated vibration patterns. Modeling results from Murdoch *et al.* (2018) suggest the lander resonance modes (generally above 10 Hz) are proportional to the square root of ground stiffness assuming a half-space below the lander, and that the ground stiffness change is two times the resonance frequency change. Here we extrapolate the results from Murdoch *et al*. (2018) to lower frequencies (3.3 and 4.1 Hz) and estimate the maximal ground stiffness changes by attributing all the daily variation of the resonance mode to ground stiffness changes. In this case, the ~5% daily changes in resonance modes at 3.3 and 4.1 Hz imply ~10% variation in near-surface ground stiffness at the foot of the lander.

On the other hand, we observe different amplitudes and phase delays of *df/f* relative to the ground temperature at different resonance frequencies. As different spectral peaks may correspond to vibration of different parts of the lander, two possibilities may explain this observation: (1) the contribution from lander structural variations differs for different resonance eigen-frequencies; (2) the different modes may have different sensitivity kernels to ground stiffness at depth and laterally.

To summarize, the observations are consistent with the hypothesis that the observed spectral peaks are lander resonance modes and suggest up to ~10% ground stiffness changes in 1-5 Hz. We note, however, that this hypothesis relies on two assumptions: (1) the lander's vibration patterns are so complicated that different spectral peaks correspond to vibrations of different parts of the lander and have different ground stiffness sensitivity, and (2) the lander resonance modes vibrate "isotropically", i.e., produce similar interference patterns in all three components. It also implies that the obvious spectral peaks in seismic data on Mars at 1-10 Hz contains little information about subsurface structures.

Hypothesis II – The Spectral Peak At ~3.3 Hz And Perhaps Others Are Associated With Site Resonance Modes

Imaging results indicate various shallow and deep interfaces with velocity contrasts on Mars (e.g., Deng & Levander 2020, Lognonné *et al.* 2020). The wind-generated lander vibration must act to some extent as a local active source, so it generates signals at certain frequencies which could interfere with reflections from subsurface interfaces. With the persistent active source signals from lander vibration, ACFs of the continuous seismic recording contain reflections from the shallow subsurface and may be analyzed further as reflection seismograms. In section

Monitoring Using ACF With An Active Source (Electronic supplement), we discuss the properties of ACFs with active source signals in detail.

We take the resonance mode at 4.1 Hz as the active source since it is the strongest persistent signal that shows similar patterns when the seismometer operates on the lander's deck and on the ground, and is well characterized by the previous study as the lander resonance mode (e.g., Lognonné *et al.* 2020). The spectrum of the seismic recording is equal to the multiplication of the source term (with a resonance mode f_2 = 4.1 Hz) and the site term that oscillates periodically at $f_1 = (N+0.5)/\Delta t$ (Equation S2a, Electronic supplement). Here Δt is the two-way travel time of waves from a subsurface reflector, and is 1.36 sec based on analysis of ACFs (Fig. 3b). This predicts f_1 = 3.3 Hz when $N = 4$ and f_1 = 4.04 Hz when $N = 5$. It implies the observation at ~3.3 Hz is dominated by the site term, while the observation at ~4.1 Hz is the convolution of the source and site terms (section Monitoring Using ACF With An Active Source, Electronic supplement). Specifically, we notice the signal at ~1.3 sec is consistent with previously observed *S*-waves based on analysis of diffused noise at 5-7 Hz (Suemoto *et al.* 2020), where there is no interference of source resonance modes that could modulate the ACF at a period of ~1.3 sec.

Interestingly, the vertical component ACFs also contain a signal at ~1.3 sec similar to the horizontal ones. This is also observed in previous studies based on diffused ambient noise at 5-7 Hz (Suemoto *et al.* 2020). While it seems straightforward to associate the two horizontal components ACFs with *S*-wave interference, this is not the case for the vertical component, although the *S*-wave signals in the vertical component could be caused by *S*-wave energy leaking to the vertical component. Three mechanisms may be responsible for energy leaking: (1) local scattering; (2) the first arriving phase in the vertical component travels as *P*-waves in the top layer (~1-2 m thick; Lognonné *et al.* 2020) and converts to *S*-waves at depth; (3) the energy transfers from horizontal directions to the vertical via the lander-ground coupling. It is difficult to derive the lander response function. However, given the lander's shape and that it is coupled with the ground through a tripod, forces applied to the lander's feet are expected intuitively to cancel out in the horizontal direction and add up in the vertical direction. Therefore, the lander response likely amplifies the vertical ground motion relative to the horizontal, resulting in energy leaking from the horizontal directions to the vertical.

It is important to point out that the active source signal at 4.1 Hz also exhibits temporal variations, either implying a change of source (lander vibration; section Hypothesis I – All Spectral Peaks Are Lander Resonance Modes) or the modulation of varying structural response (section Properties Of ACF With An Active Source, Electronic supplement). Previous studies noted that temporal changes in source spectra may introduce a bias to *dt/t* measurements in some cases (e.g., coda wave interferometry using the stretching method; Zhan *et al*. 2013). We illustrate in section Monitoring With ACF (Electronic supplement) that the estimated *dt/t* values in this study are insensitive to temporal changes of the source dominant frequency f_c. Therefore, the observed *dt/t* and *df/f* at ~3.3 Hz could represent *S*-wave velocity variation between the surface to an interface below. Estimation based on velocity models from Lognonné *et al*. (2020) then indicates that the two-way travel time of ~1.3 sec corresponds to a ~200-m-deep reflector, and the ~5% travel time variation represents material changes averaged in the top 200 m considering $dt/t=-dv/v$.

The variation of higher spectral peaks, if they are not associated with the lander resonance modes, could indicate structural variations at different depth ranges. The wave reflected from a shallower interface (< 200 m) may dominate the ACFs at higher frequencies, considering the stronger attenuation of higher frequency waves. This implies the velocity change amplitude decreases while the phase delay relative to the temperature increases with depth. However, we do not observe clear signals in time-domain ACFs possibly due to the low signal-to-noise ratio.

Therefore, the observations are also compatible with the hypothesis that some of the observed spectral peaks, especially the one at ~3.3 Hz, are associated with site resonance modes. We note that the ACF is a convolution of source (lander vibration) and structural information, and the observed *dt/t* could be convolved with the temporal variations of the lander. We conclude the estimated ~5% *dt/t* averaged in the top ~200 m may represent an upper limit of structural changes in that layer.

Can We Distinguish Between The Two Hypotheses?

As illustrated in the above sections, both hypotheses are compatible with the ACF results and previous studies. The key is the origin of the ~1.3-sec signal or the 3.3 Hz spectral peak in ACFs. We cannot reject the first hypothesis since the vibration patterns of the lander are too complicated to model accurately and the driving force (e.g., atmospheric events, wind activities) is highly variable on Mars (e.g., Murdoch *et al.* 2017, Morgan *et al.* 2018). Therefore, we aim to investigate whether additional observational results can rule out the second hypothesis.

A strong correlation is observed between the spectral peak amplitude and wind speed (e.g., Lognonné *et al.* 2020), but this does not exclude the possible contribution from the interference of seismic waves in subsurface layers. If a resonance mode (e.g., at ~3.3 Hz) corresponds to the interference of the source signal (e.g., at ~4.1 Hz) and its reflection, the amplitude of the resonance mode is also expected to correlate with the wind speed driving the active source amplitude (section Monitoring Using ACF With An Active Source, Electronic supplement), which is proportional to the wind speed.

Before being deployed on the ground, the seismometer operated on the deck of the lander for ~2 weeks during the afternoons and early evenings on Mars. We expect the on-deck data to be distorted, if not dominated, by the lander response (i.e. a transfer function associated with the coupling between the lander and ground), though the sensor on the deck is capable of recording waves from underground structures (Panning & Kedar 2019, Panning *et al.* 2020). In section Comparison Of The On-deck And On-ground Data (Electronic supplement), we compare the on-ground and on-deck data, in terms of the travel time variation in ACFs and spectral peak properties at ~3.3 and ~4.1 Hz, and demonstrate that these results are also consistent with both hypotheses.

Without independent information about the source or the subsurface structure, there is no clear way to distinguish the two hypotheses. This stems from the fact that the frequency domain resonances (e.g., f_1 and f_2) and time domain arrivals (Δt) in ACFs are coupled with each other via $\Delta t=N/(f_2-f_1)$ as interference of source resonance modes, and $f_1=f_2-N/\Delta t$ as interference of seismic waves in subsurface layers.

We conclude that the observations from ACFs likely represent a sum of the source and site effects. The observed dt/t and df/f indicate a combination of lander vibration change (lander structural change, and the near-surface ground stiffness change affecting lander-ground coupling), along with subsurface structural variations averaged in the top ~200 m. The estimated near-surface ground stiffness change is ~ 10% in 1-5 Hz and the average structural variation in the top ~200 m is ~5%. Both estimates represent upper limit values.

Velocity Variation Induced By Thermoelastic Strain

Regardless of which hypothesis holds, the daily variations (dt/t and $-df/f$) with a similar shape and phase delay relative to the ground temperature recording imply that a major driving mechanism is thermoelastic strain in the lander and subsurface structures. Estimating quantitatively the thermoelastic strain requires numerical simulations involving various poorly constrained parameters of the landers and subsurface structures. We therefore focus on thermoelastic strain at the subsurface using a simple analytical solution in an elastic half-space that requires a few basic parameters (Berger 1975, Ben-Zion & Leary 1986). The amplitude of thermoelastic strain (section Thermoelastic Strain, Electronic supplement) decreases significantly in the top ~20 m and remains almost constant at 20-200 m. On the other hand, material strength increases with increasing confining pressure (e.g., Nur & Simmons 1969, TenCate *et al.* 2004, Pasqualini *et al.* 2007). Therefore, the velocity variations likely concentrate in the top ~20 m weak regolith or shallower materials. Indeed, analysis of borehole data on Earth shows that temporal changes tend to concentrate in the top few meters to tens of meters (Rubinstein 2011, Bonilla *et al.* 2019, Qin *et al.* 2020). We therefore estimate the travel time variation in the top 20 m.

Richter *et al*. (2014) estimated the level of velocity variation induced by thermoelastic strain via:

$$\frac{dv}{v}(x,y,t) = b\alpha\frac{\partial\rho v^2}{\partial\sigma}T(x,y=0,t)[2e^{-(1+i)\gamma y} - \frac{(1+\nu)(1-i)k}{\gamma}e^{-ky}] \quad (1)$$

Here x, y represent the horizontal and vertical coordinates, ω is the angular frequency, $T(x,y = 0,t)$ is the surface temperature field, κ, α and ν represent the thermal diffusivity, linear expansion coefficient and Poisson's ratio of the elastic half-space, respectively, b is equal to $\frac{1+\nu}{1-\nu}$ for S waves, $k = 2\pi/\lambda$ is the wavenumber of the surface temperature field with λ being the wavelength, and γ is the real part of $k \cdot (1 + \frac{i\omega}{\kappa k^2})^{1/2}$.

The travel time variation dt from surface to a certain depth H is obtained via

$$dt = \int_0^H \Delta s \ dh = \int_0^H -\frac{\Delta v}{v^2}\ dh \quad (2)$$

Since the material properties $(v, \upsilon, \frac{\partial \rho v^2}{\partial \sigma}, \alpha, \kappa)$ on Mars are poorly constrained and can vary by two orders of magnitude (Morgan *et al.* 2018), we simplify the analysis assuming constant (average) properties over depth. This leads to

$$dt = \frac{b\alpha \frac{\partial \rho v^2}{\partial \sigma} T(x,y=0,t)}{\gamma v} \cdot (1-i) \cdot \left[e^{-(1+i)\gamma H} - 1 + (1+\upsilon)(1-e^{-kH})\right] \tag{3}$$

We estimate dt in the top 20 m with parameters from previous studies (Morgan *et al.* 2018, Compaire *et al.* 2022) shown in Table 1. Since we calculated dt/t using the average value during night time as the reference, $T(x, y = 0, t)$ is also the surface temperature relative to the night time, which is ~100 ℃ (Fig. 1a). For shallow materials at Mars, the thermal diffusivity κ is on the order of 10^{-8} m^2/s, and the thermal conductivity is ~10^{-2} W m^{-1} K^{-1}, close to the pore-filling CO_2 gas conductivity (Morgan *et al.* 2018). We thus assume a linear expansion coefficient α on the order of 10^{-3} °C^{-1}. The wavelength of the temperature field is comparable to that of the topography variation (Ben-Zion and Leary, 1986), which is expected to be over 10 km at the relatively flat InSight landing site. The amplitude of thermoelastic strain at shallow depth is not sensitive to λ when $\lambda > 500\ m$ or the Poisson's ratio υ in the range of 0.1-0.5 (Figs S10-S11, Electronic supplement). We therefore set $\upsilon = 0.3$, and $\lambda = 15\ km$. The average S-wave velocity v and $\frac{\partial \rho v^2}{\partial \sigma}$ follow directly from Compaire *et al*. (2022). Since $\kappa \ll \omega/k^2$, we approximate γ as $(\omega/2\kappa)^{1/2}$.

With Equation (3) and the parameters in Table 1, the travel time variation in the top 20 m relative to mean night value is estimated to be $dt = 0.03\ sec$ with a phase delay of 3 hours relative to the surface temperature. The corresponding dt/t is 4.4% if the travel time variation is averaged over the top 200 m (Δt=1.36 sec, Fig. 3b). If we assume no structure variations below 20 m, and the S-wave travel time in the top 20 m is ~0.2 sec with an average velocity of 100 m/s, the upper limit of *dt/t* in the top 20 m is ~15%. Our observations (section Monitoring Subsurface Structures

Using ACFs) also suggest that the upper limit of ground stiffness change is ~10% if all the spectral peaks are lander resonance modes, and that the *dt/t* variation of *S*-wave is ~5% averaged in the top ~200 m if the 3.3 Hz spectral peak is associated with interference of direct and reflected seismic waves from subsurface layers. These values are consistent with those predicted from Equation (3), considering the uncertainties of parameters.

The phase of dt is dominated by the second term, which is 1/8 of the temperature period. This predicts a 3-hour delay for daily variations, larger than our observation (~50 min). There are four possible reasons for this difference. First, there are multiple harmonics in the temperature field on Mars (Fig. S13, Electronic supplement) in addition to 24 hr. The shorter period components at 12 hr, 8 hr and 6 hr generate smaller phase delays, reducing the superposed phase delay. Second, our observations are combined effects from variations of the lander vibration and subsurface structure. Since the lander material is expected to deform faster with temperature than the ground materials, the observed phase delay is smaller than that predicted only from subsurface structure variations. Third, our observation is an apparent phase delay t_0, and the true delay could be t_0 plus multiples of one Martian day. In addition, Equation (3) does not consider a possible decoupled surface layer which may introduce a further phase delay to the subsurface velocity variations (Ben-Zion & Leary 1986). Fourth, the relationship between velocity variation and strain level depends on the material, confining pressure, and fluid content, while Equation (3) adopted a simplified model. Therefore, the amplitude and phase of predicted and observed dt/t values are of the same order, with some discrepancies that may be caused by parameter uncertainties, complex relation between strain and velocity variations, possible existence of a decoupled surface layer, and possible variations of the lander properties.

Discussion

We analyze the temporal patterns of ACFs using seismic data recorded on Mars. The signal at ~1.3 sec in ACFs shows ~5% daily variation (*dt/t*), and varies similarly to the daily ground temperature variation with ~50 min apparent phase difference. The spectral peaks at 3.3, 4.1, 6.8, 8.5 and 9.8 Hz also show daily variations (*-df/f*) between 5-25% with phase delays of ~45-20 min relative to the ground temperature. The correlation and phase delays of *dt/t* and *-df/f* with the ground temperature suggest that the most likely driving mechanism is thermoelastic strain. The analyzed ACFs represent convolved effects of the lander vibrations and subsurface structures, so two end-member mechanisms can explain the observations: (1) all the spectral peaks are lander resonance modes, and the observed signal at ~1.3 sec in the ACFs variations result from the interference of resonance modes; (2) the signal at ~1.3 sec in the ACF is associated with subsurface reflected *S*-waves and the spectral peak at 3.3 Hz is generated by the interference between the lander resonance at 4.1 Hz and its reflection.

For the first mechanism, the interference of lander resonance modes at 3.3 and 4.1 Hz generates the signal at ~1.3 sec, and variations of ACF (*dt/t* and *df/f*) reflect variations of the lander vibration induced by its structural and near-surface ground stiffness changes affecting the lander-ground coupling. Both effects are generated by temperature variations, since the *dt/t* and *df/f* correlate well with the ground temperature. Given the complicated lander structure (e.g., solar panels and tripod), it is almost impossible to quantify how resonance frequencies of wind-related lander vibrations vary with the thermal expansion/compaction of the lander. Considering the phase delay of *df/f* and *dt/t* relative to the temperature, variation of ground stiffness should have considerable contribution to the observed changes. Estimation using a simplified model (Murdoch *et al*. 2018) indicates up to ~10% ground stiffness changes based on variations at 3.3 and 4.1 Hz. Variations of other resonance modes increase with frequency, while the phase delays relative to the ground temperature decrease (Fig. 5). This may indicate higher-frequency modes have shallower sensitivity kernels to ground stiffness, which is consistent with the depth distribution of thermoelastic strain, i.e., thermal expansion of unconsolidated materials at a shallower depth is more significant and responds faster to fluctuations in incoming solar radiation. However, it is also possible that these high-frequency modes correspond to resonances of different parts of the lander, and the corresponding variations and phase delays represent changes in different components of the lander.

For the second mechanism, the signal at ~1.3 sec in the ACF is associated with subsurface reflected *S*-waves. Considering the lander vibration with a dominant frequency at 4.1 Hz as a persistent active source, the ~3.3 Hz spectral peak is related to the interference of direct and reflected *S*-waves. Since variations in the frequency content of the active source do not affect the travel time of the reflected phase retrieved from ACF (Electronic supplement), the observed ~5% daily variations in travel time of the reflected signal in ACF reflect changes in subsurface velocity structures beneath the lander. Based on the S-wave velocity model of Lognonné *et al*. (2020), the observation suggests ~5% daily velocity variation averaged in the top ~200 m. Given the good correlation and ~1-hour phase delay between the observed *dt/t* and ground temperature, the dominating mechanism is likely thermoelastic strain. Considering the amplitude of thermoelastic strain decreases significantly with depth, velocity changes should concentrate in shallow materials. Assuming the regolith layer in the top ~20 m accommodates most of the daily variations in the two-way travel time of the reflected signal, the daily variation in S-wave velocity is ~15%, which agrees well with the predicted value by modeling thermoelastic strain with representative parameters.

The two mechanisms differ in the assumption of whether the spectral peaks, and especially the one at 3.3 Hz, are resonance modes exclusively from lander vibrations. It might be helpful to compare synchronous on-deck and on-ground seismic recordings if they are available. Future studies of resonance frequencies of the lander vibration on Mars, using for example numerical modeling and laboratory experiments, may also help distinguish which mechanism is more probable. Murdoch *et al*. (2018) used a simplified mechanical model to predict lander resonance modes at frequencies lower than 1 Hz or higher than 10 Hz. However, they are unable to reproduce the lander resonance mode at 4.1 Hz observed in the seismic recording on Mars, suggesting the necessity of using a more complicated mechanical model to better simulate the lander vibration. Moreover, the environmental conditions on Mars (e.g. wind, temperature) and the coupling between the lander's foot and near-surface materials may also affect the accuracy of the lander resonance mode simulation.

In summary, the two end-member mechanisms attribute the observed daily variations in ACFs to changes in the active source and subsurface velocity structure, respectively. As discussed in the section "Can We Distinguish Between The Two Hypotheses?", it is not possible currently to distinguish the two mechanisms using the available data, and the observed ACF variations likely involve contributions from the source (lander vibration) and the subsurface structure changes. It is difficult to estimate accurately the daily velocity variation of shallow materials on Mars using ACFs. However, the inferred daily subsurface changes, i.e., ~10% in ground stiffness at 3.3-4.1 Hz or ~15% in S-wave velocity averaged over the top ~20 m, still provide useful upper bound variations of near-surface materials on Mars.

Conclusions

Based on analysis of the high-frequency (1-5 Hz) ACFs of the seismic data on Mars, we observe ~5% daily travel time variation (*dt/t*) in the signal at ~1.3 sec. The observed *dt/t* has a similar shape as the daily ground temperature variation with ~50 min apparent phase difference. Similar temporal patterns are observed for spectral peaks at 3.3, 4.1, 6.8, 8.5 and 9.8 Hz with peak-to-peak daily variations (*-df/f*) between 5-25% and phase delays of ~45-20 min relative to the ground temperature. We conclude that the ACF-based results include contributions from the lander structural variations, near-surface ground stiffness changes affecting the lander-ground coupling, and subsurface structural variations (especially in the top ~20 m) induced by thermoelastic strain. The daily velocity change in response to surface temperature on Mars is significantly larger than those resolved on Earth, and may be amplified due to the combined effects of large temperature variation of ~100 ºC, low barometric pressure of ~700 Pa, high wind speeds that may induce seismic motion at depth (Johnson *et al.* 2019), and the local structure with extremely low *S*-wave velocities (<100 m/s) in the top few meters. The results highlight the need to characterize source properties in ACF analysis, and the importance of seismic monitoring in planetary missions for a better understanding of the properties and dynamics of sub-surface materials.

DATA AND RESOURCES

The InSight seismic data is available on the Incorporated Research Institutions for Seismology (IRIS) Data Management Center (InSight Mars SEIS Data Service, 2019, www.iris.edu/hq/sis/insight). The ground temperature data is downloaded from the following URL (https://pds-geosciences.wustl.edu/insight/urn-nasa-pds-insight_rad/data_derived/). The wind, air temperature and pressure data are downloaded from https://atmos.nmsu.edu/data_and_services/atmospheres_data/INSIGHT/insight.html#Selecting_Data.

ACKNOWLEDGEMENTS

We acknowledge NASA, CNES, their partner agencies and Institutions (UKSA, SSO, DLR, JPL, IPGP-CNRS, ETHZ, IC, MPS-MPG) and the flight operations team at JPL, SISMOC, MSDS, IRIS-DMC and PDS for providing SEED SEIS data (InSight Mars SEIS Data Service, 2019) and ground temperature data. The study was supported by the U.S. Department of Energy (award DE-SC0016520). Lei Qin was also supported by the Fundamental Research Funds for the Central Universities, China University of Geosciences (Wuhan) (NO. 106-162301212665). The manuscript benefited from constructive comments of the Associate Editor Zefeng Li and two anonymous referees.

References

Banerdt, W.B., Smrekar, S.E., Banfield, D., Giardini, D., Golombek, M., Johnson, C.L., Lognonné, P., *et al.* (2020) Initial results from the InSight mission on Mars. *Nat. Geosci.*, **13**, 183–189, Springer US. doi:10.1038/s41561-020-0544-y

Ben-Zion, Y. & Allam, A.A. (2013) Seasonal thermoelastic strain and postseismic effects in Parkfield borehole dilatometers. *Earth Planet. Sci. Lett.*, **379**, 120–126, Elsevier B.V. doi:10.1016/j.epsl.2013.08.024

Ben-Zion, Y. & Leary, P. (1986) Thermoelastic strain in a half-space covered by unconsolidated material. *Bull. Seismol. Soc. Am.*, **76**, 1447–1460.

Berger, J. (1975) A Note on Thermoelastic Strains and Tilts. *J. Geophys. Res.*, **80**, 274–277.

Bonilla, L.F., Guéguen, P. & Ben-Zion, Y. (2019) Monitoring coseismic temporal changes of shallow material during strong ground motion with interferometry and autocorrelation. *Bull. Seismol. Soc. Am.*, **109**, 187–198. doi:10.1785/0120180092

Brenguier, F., Shapiro, N.M., Campillo, M., Ferrazzini, V., Duputel, Z., Coutant, O. & Nercessian, A. (2008) Towards forecasting volcanic eruptions using seismic noise. *Nat. Geosci.*, **1**, 126–130. doi:10.1038/ngeo104

Claerbout, J.F. (1968) Synthesis of a layered medium from its acoustic transmission response. *Geophysics*, **33**, 264–269.

Compaire, N., Margerin, L., Monnereau, M., Garcia, R.F., Lange, L., Calvet, M., Dahmen, N.L., *et al.* (2022) Seasonal variations of subsurface seismic velocities monitored by the SEIS-InSight seismometer on Mars. *Geophys. J. Int.*, **229**, 776–799. doi:10.1093/gji/ggab499

Dahmen, N.L., Zenhäusern, G., Clinton, J.F., Giardini, D., Stähler, S.C., Ceylan, S., Charalambous, C., *et al.* (2021) Resonances and Lander Modes Observed by InSight on Mars (1–9 Hz). *Bull. Seismol. Soc. Am.*, **111**, 2924–2950. doi:10.1785/0120210056

Deng, S. & Levander, A. (2020) Autocorrelation Reflectivity of Mars. *Geophys. Res. Lett.*, **47**. doi:10.1029/2020GL089630

De Plaen, R., Cannata, A., Cannavo', F., Caudron, C., Lecocq, T. & Francis, O. (2019) Temporal changes of seismic velocity caused by volcanic activity at Mt. Etna revealed by the autocorrelation of ambient seismic noise. *Front. Earth Sci.*, **6**, 1–11. doi:10.3389/feart.2018.00251

Froment, B., Campillo, M., Chen, J.H. & Liu, Q.Y. (2013) Deformation at depth associated with the 12 May 2008 MW 7.9 Wenchuan earthquake from seismic ambient noise monitoring. *Geophys. Res. Lett.*, **40**, 78–82. doi:10.1029/2012GL053995

Johnson, C.W., Fu, Y. & Bürgmann, R. (2017) Stress Models of the Annual Hydrospheric, Atmospheric, Thermal, and Tidal Loading Cycles on California Faults: Perturbation of Background Stress and Changes in Seismicity. *J. Geophys. Res. Solid Earth*, **122**, 10,605-10,625. doi:10.1002/2017JB014778

Johnson, C.W., Meng, H., Vernon, F.L. & Ben-Zion, Y. (2019) Characteristics of Ground Motion Generated by Wind Interaction With Trees, Structures, and Other Surface Obstacles. *J. Geophys. Res. Solid Earth*. doi:10.1029/2018JB017151

Karabulut, H. & Bouchon, M. (2007) Spatial variability and non-linearity of strong ground motion near a fault. *Geophys. J. Int.*, **170**, 262–274. doi:10.1111/j.1365-246X.2007.03406.x

Kim, D., Davis, P., Lekić, V., Maguire, R., Compaire, N., Schimmel, M., Stutzmann, E., *et al.* (2021) Potential Pitfalls in the Analysis and Structural Interpretation of Mars' Seismic Data from InSight. *Bull. Seismol. Soc. Am.*, 1–21. doi:10.1785/0120210123

Kim, D. & Lekic, V. (2019) Groundwater Variations From Autocorrelation and Receiver Functions. *Geophys. Res. Lett.*, **46**, 13722–13729. doi:10.1029/2019GL084719

Knapmeyer-Endrun, B., Panning, M.P., Bissig, F., Joshi, R., Khan, A., Kim, D., Lekić, V., *et al.* (2021) Thickness and structure of the martian crust from InSight seismic data. *Science (80-.).*, **373**, 438–443. doi:10.1126/science.abf8966

Lin, F.C., Li, D., Clayton, R.W. & Hollis, D. (2013) High-resolution 3D shallow crustal structure in Long Beach, California: Application of ambient noise tomography on a dense seismic array. *Geophysics*, **78**. doi:10.1190/geo2012-0453.1

Lognonné, P., Banerdt, W.B., Giardini, D., Pike, W.T., Christensen, U., Laudet, P., Raucourt, S. de, *et al.* (2019) SEIS: Insight's Seismic Experiment for Internal Structure of Mars. *Space Sci. Rev.*, **215**. doi:10.1007/s11214-018-0574-6

Lognonné, P., Banerdt, W.B., Pike, W.T., Giardini, D., Christensen, U., Garcia, R.F., Kawamura, T., *et al.* (2020) Constraints on the shallow elastic and anelastic structure of Mars from InSight seismic data. *Nat. Geosci.*, **13**, 213–220. doi:10.1038/s41561-020-0536-y

Lu, Y. & Ben-Zion, Y. (2022) Regional seismic velocity changes following the 2019 Mw7.1 Ridgecrest, California earthquake from autocorrelations and P/S converted waves. *Geophys. J. Int.*, **228**, 620–630. doi:10.1093/gji/ggab350

Mao, S., Campillo, M., Hilst, R.D. van der, Brenguier, F., Stehly, L. & Hillers, G. (2019) High Temporal Resolution Monitoring of Small Variations in Crustal Strain by Dense Seismic Arrays. *Geophys. Res. Lett.*, **46**, 128–137. doi:10.1029/2018GL079944

Morgan, P., Grott, M., Knapmeyer-Endrun, B., Golombek, M., Delage, P., Lognonné, P., Piqueux, S., *et al.* (2018) A Pre-Landing Assessment of Regolith Properties at the InSight Landing Site. *Space Sci. Rev.*, **214**, Springer Nature B.V. doi:10.1007/s11214-018-0537-y

Murdoch, N., Alazard, D., Knapmeyer-Endrun, B., Teanby, N.A. & Myhill, R. (2018) Flexible Mode Modelling of the InSight Lander and Consequences for the SEIS Instrument. *Space Sci. Rev.*, **214**, Springer Nature B.V. doi:10.1007/s11214-018-0553-y

Murdoch, N., Mimoun, D., Garcia, R.F., Rapin, W., Kawamura, T., Lognonné, P., Banfield, D., *et al.* (2017) Evaluating the Wind-Induced Mechanical Noise on the InSight Seismometers. *Space Sci. Rev.*, **211**, 429–455, Springer Science+Business Media Dordrecht. doi:10.1007/s11214-016-0311-y

Murphy, J.R., Davis, A.H. & Weaver, N.L. (1971) AMPLIFICATION OF SEISMIC BODY WAVES BY LOW-VELOCITY SURFACE LAYERS. *Bull. Seismol. Soc. Am.*, **61**, 109–145.

Nur, A. & Simmons, G. (1969) The effect of saturation on velocity in low porosity rocks. *Earth Planet. Sci. Lett.*, **7**, 183–193. doi:10.1016/0012-821X(69)90035-1

Oren, C. & Nowack, R.L. (2017) Seismic body-wave interferometry using noise autocorrelations for crustal structure. *Geophys. J. Int.*, **208**, 321–332. doi:10.1093/gji/ggw394

Panning, M.P. & Kedar, S. (2019) Seismic response of the Mars Curiosity Rover: Implications for future planetary seismology. *Icarus*, **317**, 373–378, Elsevier. doi:10.1016/j.icarus.2018.06.017

Panning, M.P., Lognonné, P., Bruce Banerdt, W., Garcia, R., Golombek, M., Kedar, S., Knapmeyer-Endrun, B., *et al.* (2017) Planned Products of the Mars Structure Service for the InSight Mission to Mars. *Space Sci. Rev.*, **211**, 611–650. doi:10.1007/s11214-016-0317-5

Panning, M.P., Pike, W.T., Lognonné, P., Banerdt, W.B., Murdoch, N., Banfield, D., Charalambous, C., *et al.* (2020) On-Deck Seismology: Lessons from InSight for Future Planetary Seismology. *J. Geophys. Res. Planets*, **125**, 1–13. doi:10.1029/2019JE006353

Pasqualini, D., Heitmann, K., TenCate, J.A., Habib, S., Higdon, D. & Johnson, P.A. (2007) Nonequilibrium and nonlinear dynamics in Berea and Fontainebleau sandstones: Low-strain regime. *J. Geophys. Res. Solid Earth*, **112**, 1–16. doi:10.1029/2006JB004264

Peng, Z. & Ben-Zion, Y. (2006) Temporal changes of shallow seismic velocity around the Karadere-Düzce branch of the north Anatolian fault and strong ground motion. *Pure Appl. Geophys.*, **163**, 567–600. doi:10.1007/s00024-005-0034-6

Phạm, T.S. & Tkalčić, H. (2017) On the feasibility and use of teleseismic P wave coda autocorrelation for mapping shallow seismic discontinuities. *J. Geophys. Res. Solid Earth*, **122**, 3776–3791. doi:10.1002/2017JB013975

Prieto, G.A., Lawrence, J.F., Chung, A.I. & Kohler, M.D. (2010) Impulse response of civil structures from ambient noise analysis. *Bull. Seismol. Soc. Am.*, **100**, 2322–2328. doi:10.1785/0120090285

Qin, L., Ben-Zion, Y., Bonilla, L.F. & Steidl, J.H. (2020) Imaging and Monitoring Temporal Changes of Shallow Seismic Velocities at the Garner Valley Near Anza, California, Following the M7.2 2010 El Mayor-Cucapah Earthquake. *J. Geophys. Res. Solid Earth*, **125**, 1–17. doi:10.1029/2019JB018070

Richter, T., Sens-Schönfelder, C., Kind, R. & Asch, G. (2014) Comprehensive observation and modeling of earthquake and temperature-related seismic velocity changes in northern Chile with passive image interferometry. *J. Geophys. Res. Solid Earth*, **119**, 4747–4765. doi:10.1002/2013JB010695

Romero, P. & Schimmel, M. (2018) Mapping the Basement of the Ebro Basin in Spain With Seismic Ambient Noise Autocorrelations. *J. Geophys. Res. Solid Earth*, **123**, 5052–5067. doi:10.1029/2018JB015498

Rubinstein, J.L. (2011) Nonlinear site response in medium magnitude earthquakes near Parkfield, California. *Bull. Seismol. Soc. Am.*, **101**, 275–286. doi:10.1785/0120090396

Schimmel, M., Stutzmann, E., Lognonné, P., Compaire, N., Davis, P., Drilleau, M., Garcia, R., *et al.* (2021) Seismic Noise Autocorrelations on Mars. *Earth Sp. Sci.*, **8**. doi:10.1029/2021EA001755

Shapiro, N.M. & Campillo, M. (2004) Emergence of broadband Rayleigh waves from correlations of the ambient seismic noise. *Geophys. Res. Lett.*, **31**, 8–11. doi:10.1029/2004GL019491

Shearer, P.M. & Orcutt, J.A. (1987) Surface and near-surface effects on seismic waves—theory and borehole seismometer results. *Bull. Seismol. Soc. Am.*, **77**, 1168–1196.

Spohn, T., Grott, M., Smrekar, S.E., Knollenberg, J., Hudson, T.L., Krause, C., Müller, N., *et al.* (2018) The Heat Flow and Physical Properties Package (HP3) for the InSight Mission.

Space Sci. Rev., **214**, The Author(s). doi:10.1007/s11214-018-0531-4

Steidl, J.H., Tumarkin, A.G. & Archuleta, R.J. (1996) What is a reference site? *Bull. Seismol. Soc. Am.*, **86**, 1733–1748. doi:https://doi.org/10.1785/BSSA0860061733

Suemoto, Y., Ikeda, T. & Tsuji, T. (2020) Temporal Variation and Frequency Dependence of Seismic Ambient Noise on Mars From Polarization Analysis. *Geophys. Res. Lett.*, **47**, 1–9. doi:10.1029/2020GL087123

TenCate, J.A., Pasqualini, D., Habib, S., Heitmann, K., Higdon, D. & Johnson, P.A. (2004) Nonlinear and nonequilibrium dynamics in geomaterials. *Phys. Rev. Lett.*, **93**, 4–7. doi:10.1103/PhysRevLett.93.065501

Xu, X.G., Konorov, S.O., Hepburn, J.W. & Milner, V. (2008) Noise autocorrelation spectroscopy with coherent Raman scattering. *Nat. Phys.*, **4**, 125–129. doi:10.1038/nphys809

Zhan, Z., Tsai, V. C., & Clayton, R. W. (2013) Spurious velocity changes caused by temporal variations in ambient noise frequency content. *Geophysical Journal International*, *194*(3), 1574-1581.

Full mailing address of each author

Lei Qin
77 Massachusetts Avenue, Building 54
Cambridge, MA 02139, US
Email: qinqiu48@gmail.com

Hongrui Qiu
77 Massachusetts Avenue, Building 54
Cambridge, MA 02139, US
Email: qiuhonrui@gmail.com

Nori Nakata
77 Massachusetts Avenue, Building 54
Cambridge, MA 02139, US
Email: nnakata@mit.edu

Sizhuang Deng
6100 Main St
Houston, TX 77005, US
Email: sd62@rice.edu

Alan Levander

6100 Main St
Houston, TX 77005, US
Email: alan@rice.edu

Yehuda Ben-Zion
3651 Trousdale Pkwy
Los Angeles, CA 90089, US
Email: benzion@usc.edu

Table 1 Parameter values used to calculate dt in the top 20 m

Parameters	v (m/s)	υ	$\frac{\partial \rho v^2}{\partial \sigma}$	κ (m^2/s)	α (°C^{-1})	T (°C)	ω (rad/h)	λ (km)
Value	100	0.3	700	10^{-8}	10^{-3}	100	$\frac{2\pi}{24}$	15

List of Figure Captions

Figure 1. Data on Mars. (a). One-day air temperature (solid black curve), ground temperature (dashed black curve), and wind data (dots color representing wind directions). (b). One-day (sol 98) EW-component continuous seismic recording band pass filtered at 1-5 Hz (gray curve). A smoothed envelope (red curve) is obtained using a 20s-long moving window, and the data divided by the smoothed envelope is shown in black. The purple dashed lines indicate 8 am-12 pm local time, where seismic recording is amplified by the wind activities. (c). Spectrogram of the EW-component data.

Figure 2. Example ACFs. (a). Time series of an example ACF at 1 PM before (black curve) and after (red curve) spectral whitening. (b). spectra of the ACFs in (a). The estimated source spectrum is illustrated in blue.

Figure 3. Results from ACF analysis of EW-component data on sol 98. (a). One-day ACFs. (b). The stack of all ACFs (black dashed curve), and an example trace at 1 PM (black solid curve). The stacked envelope for all ACFs (red curve) shows three local maxima labeled by their lapse times. Blue horizontal lines show the cross-correlation time window.

Figure 4. (a). Temporal patterns of travel time (*dt/t*), linearly scaled ground temperature (magenta dots), and the best fitting linearly scaled ground temperature curve ($g(T; a, b, t_0)$; red curve). Gaps during the Martian night result from low-quality ACFs. (b). The misfit function (L_2 norm of $g(T; a, b, t_0) - dt/t$) in parameter space. The white cross indicates the best fitting parameters that generate the minimal misfit.

Figure 5. (a). Spectrogram of the ACFs calculated using the unfiltered EW component recording. Five resonance frequencies are observed and labeled with black curves (at ~3.3, ~4.1, ~6.8, ~8.5 and ~9.8 Hz). (b). Peak frequency variations *-df/f* (black solid curves) from EW component ACFs at 3.3, 4.1, 6.8, 8.5, and 9.8 Hz, and the best fitting curves ($g(T; a, b, t_0)$; red solid curves). The reference peak frequencies and best fitting time delays are labeled for each panel.

Figures and captions

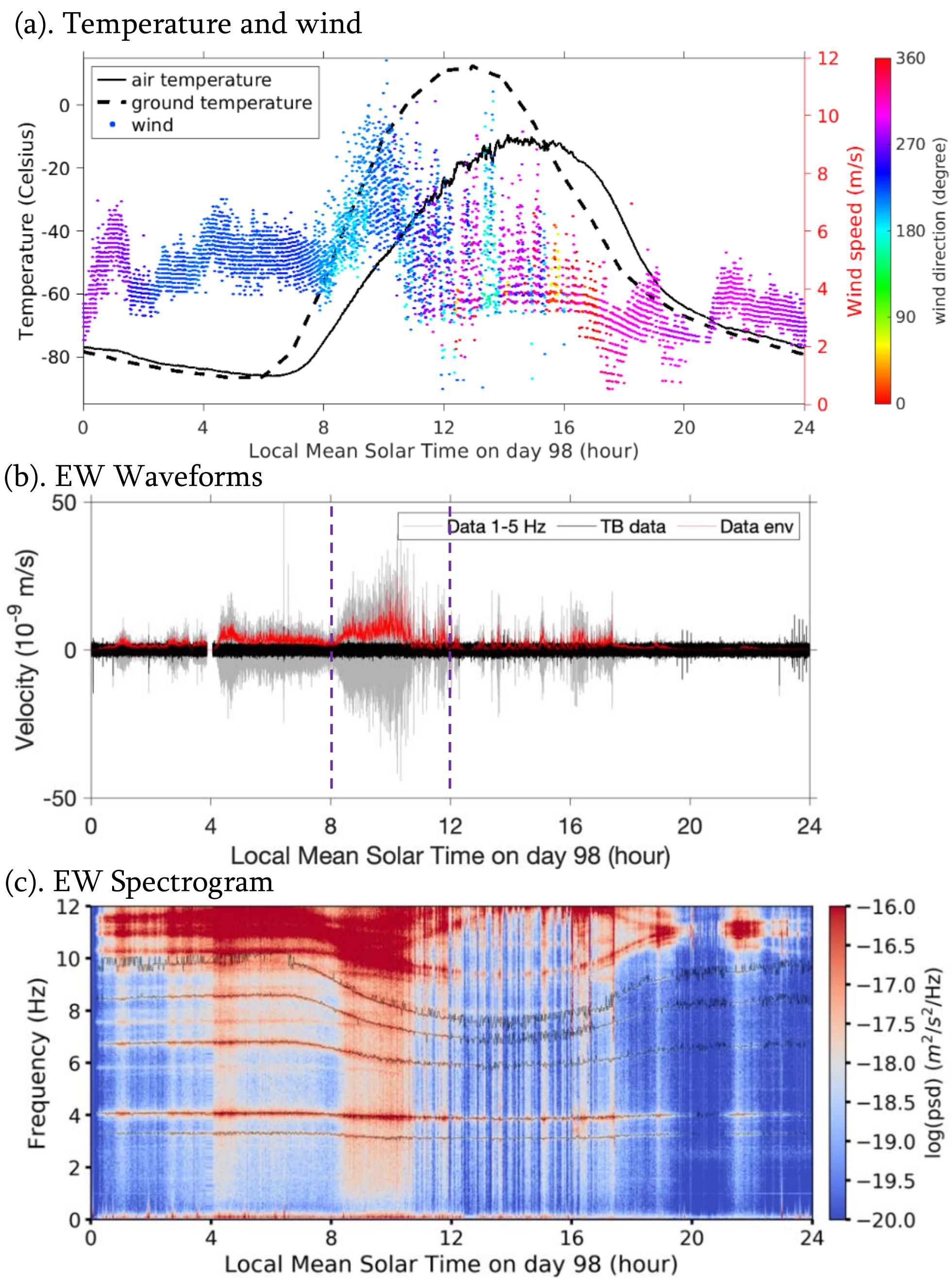

Figure 1. Data on Mars. (a). One-day air temperature (solid black curve), ground temperature (dashed black curve), and wind data (dots color representing wind directions). (b). One-day (sol 98) EW-component continuous seismic recording band pass filtered at 1-5 Hz (gray curve). A smoothed envelope (red curve) is obtained using a 20s-long moving window, and the data divided

by the smoothed envelope is shown in black. The purple dashed lines indicate 8 am-12 pm local time, where seismic recording is amplified by the wind activities. (c). Spectrogram of the EW-component data.

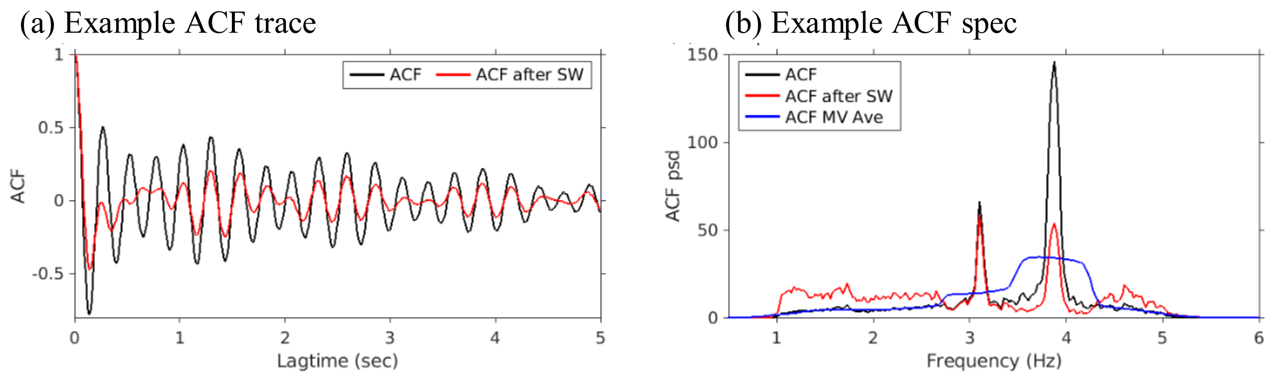

Figure 2. Example ACFs. (a). Time series of an example ACF at 1 PM before (black curve) and after (red curve) spectral whitening. (b). spectra of the ACFs in (a). The estimated source spectrum is illustrated in blue.

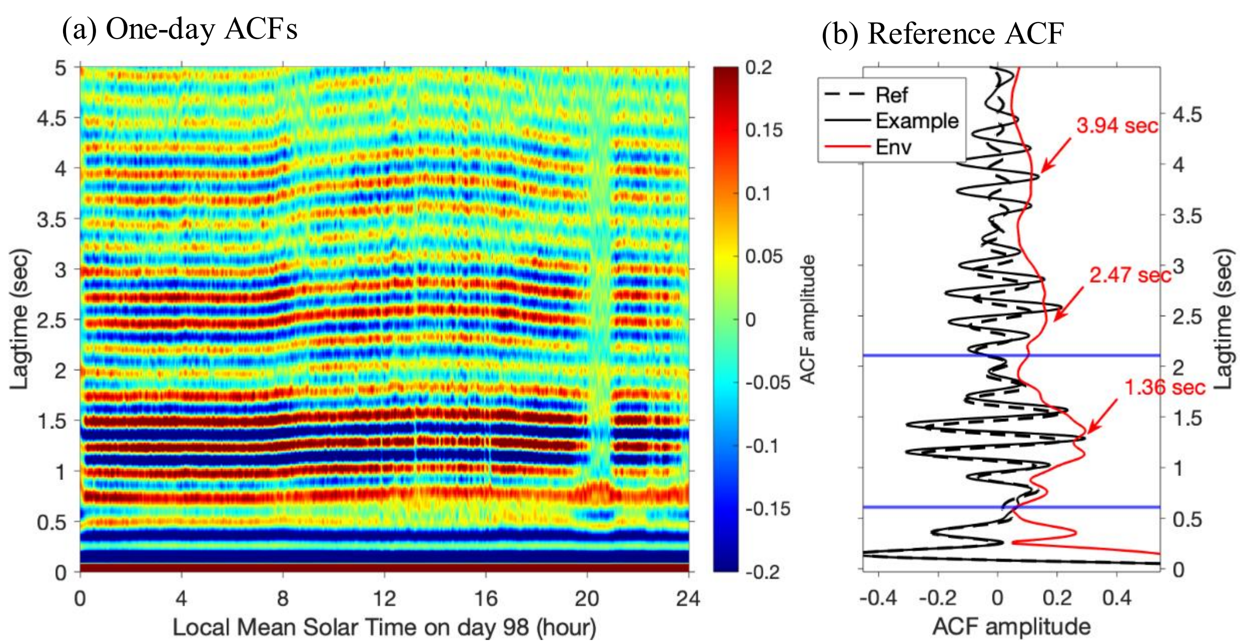

Figure 3. Results from ACF analysis of EW-component data on sol 98. (a). One-day ACFs. (b). The stack of all ACFs (black dashed curve), and an example trace at 1 PM (black solid curve). The stacked envelope for all ACFs (red curve) shows three local maxima labeled by their lapse times. Blue horizontal lines show the cross-correlation time window.

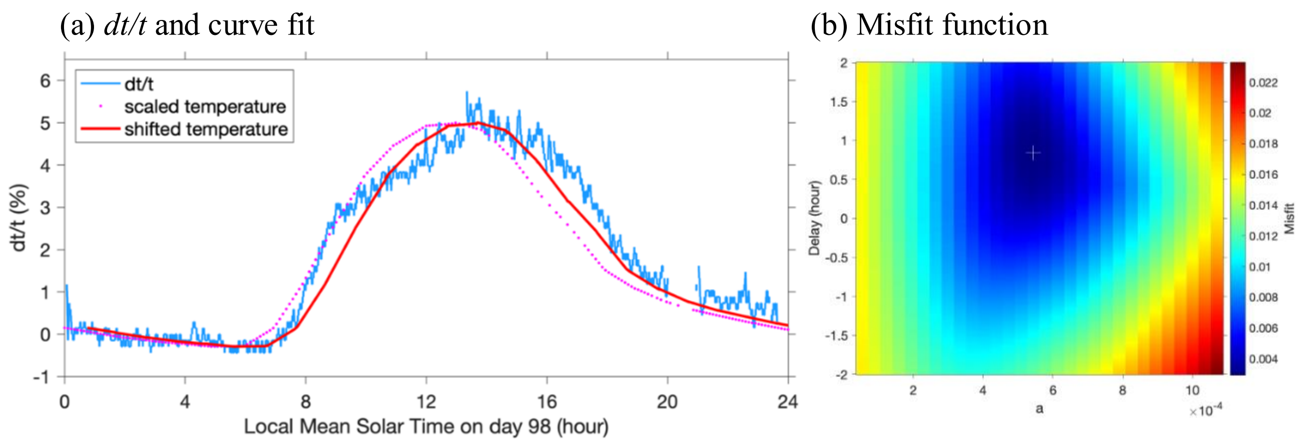

Figure 4. (a). Temporal patterns of travel time (*dt/t*), linearly scaled ground temperature (magenta dots), and the best fitting linearly scaled ground temperature curve ($g(T; a, b, t_0)$; red curve). Gaps during the Martian night result from low-quality ACFs. (b). The misfit function (L_2 norm of $g(T; a, b, t_0) - dt/t$) in parameter space. The white cross indicates the best fitting parameters that generate the minimal misfit.

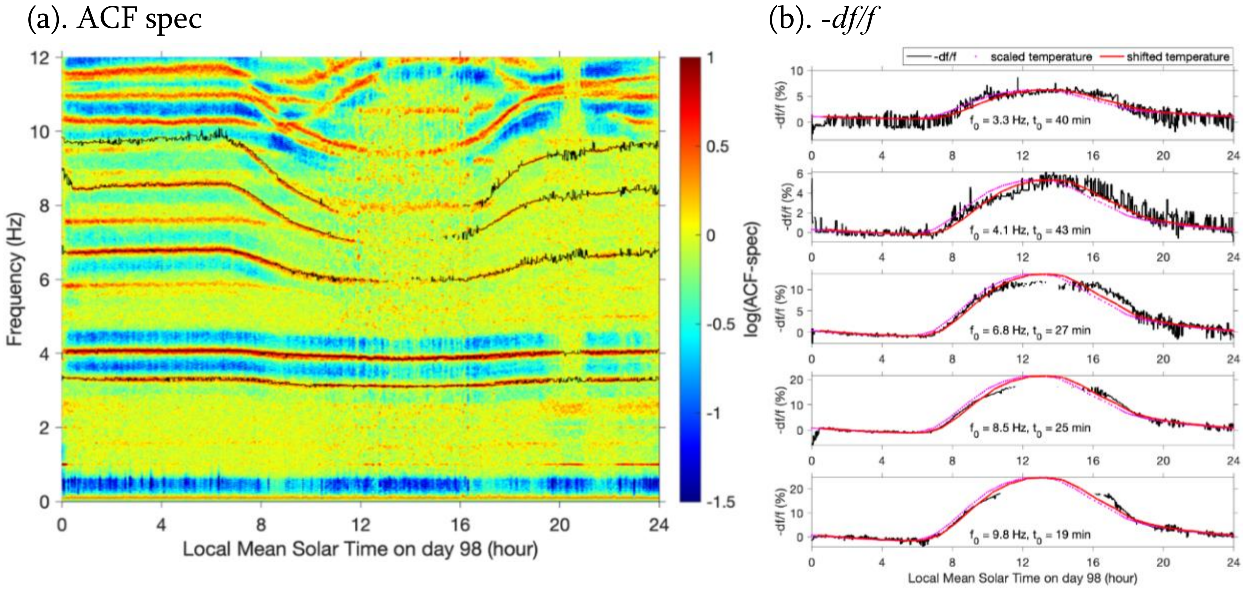

Figure 5. (a). Spectrogram of the ACFs calculated using the unfiltered EW component recording. Five resonance frequencies are observed and labeled with black curves (at ~3.3, ~4.1, ~6.8, ~8.5 and ~9.8 Hz). (b). Peak frequency variations *-df/f* (black solid curves) from EW component ACFs at 3.3, 4.1, 6.8, 8.5, and 9.8 Hz, and the best fitting curves ($g(T; a, b, t_0)$; red solid curves). The reference peak frequencies and best fitting time delays are labeled for each panel.

Electronic supplement

Variable daily autocorrelation functions of high frequency seismic data on Mars

Lei Qin[1,2], Hongrui Qiu[2*], Nori Nakata[2], Sizhuang Deng[3], Alan Levander[3], Yehuda Ben-Zion[4,5]

[1]Institute of Geophysics and Geomatics, China University of Geosciences, Wuhan, China

[2]Earth, Atmospheric and Planetary Sciences, Massachusetts Institute of Technology, Cambridge, MA, USA

[3]Department of Earth, Environmental and Planetary Sciences, Rice University, Houston, TX, USA

[4]Department of Earth Sciences, University of Southern California, Los Angeles, CA, USA

[5]Southern California Earthquake Center, University of Southern California, Los Angeles, CA, USA

*Corresponding author: Hongrui Qiu (qiuhonrui@gmail.com)

Summary

The following sections contain supplementary material to the main manuscript. We first show results from NS and vertical components on sol 98. Then in section Monitoring Using ACF With An Active Source, we present properties of the autocorrelation function (ACF) with an active source, and illustrate that changes of source frequency content does not affect our travel time variation measurements based on the cross-correlation of ACFs. In section Comparison Of The On-deck And On-ground Data, we show results from seismic data on the deck. In section Thermoelastic Strain, we discuss properties of thermoelastic strain and present its amplitude with different thermophysical parameters. We also present the power spectral density of the surface temperature field on Mars in Fig. S13.

NS And Vertical Component Results On Sol 98

In this section, we present the ACF analysis results from NS and vertical components (Figs. S1-S3), which are similar to those from the EW component.

Monitoring Using ACF With An Active Source

Properties Of ACF With An Active Source

When signals from an active source are reflected from an interface and recorded by the surface station, the surface seismic recording $D(t)$, including the direct signal $S(t)$ and its reflection, can be written as:

$$D(t) = S(t) + \delta \cdot S(t - \Delta t), \tag{S1a}$$

where $|\delta| < 1$ is the reflection coefficient, and Δt is the two-way travel time. Here we consider the case when there is only one dominant reflected signal (i.e., the amplitude of reflection from the major reflector is much larger than those from other reflectors). Equation (1a) can be written in the frequency domain as:

$$\widetilde{D}(\omega) = \tilde{S}(\omega) + \delta \cdot \tilde{S}(\omega)e^{i\omega\Delta t} = \tilde{S}(\omega) \cdot \left(1 + \delta \cdot e^{i\omega\Delta t}\right), \tag{S1b}$$

where $\widetilde{D}(\omega)$ and $\tilde{S}(\omega)$ represent the Fourier transforms of $D(t)$ and $S(t)$ at angular frequency ω, respectively. The ACF of $D(t)$ in the frequency domain, $\tilde{R}(\omega)$, can be written as

$$\begin{aligned}\tilde{R}(\omega) = \widetilde{D}(\omega) \cdot \widetilde{D}^{*}(\omega) = \left|\tilde{S}(\omega)\right|^{2} \cdot \left(1 + \delta^{2} + \delta \cdot e^{i\omega\Delta t} + \delta \cdot e^{-i\omega\Delta t}\right) = \\ \left|\tilde{S}(\omega)\right|^{2} \cdot [1 + \delta^{2} + 2\delta \cdot \cos\cos(\omega\Delta t)] = \left|\tilde{S}(\omega)\right|^{2} \cdot C_{\delta}(\omega, \Delta t).\end{aligned} \tag{S2a}$$

The phase spectrum of ACF is zero at all frequencies, while the amplitude spectrum is a multiplication of a source term $\left|\tilde{S}(\omega)\right|^{2}$ and a site term $C_{\delta}(\omega, \Delta t)$ related to the interference between the direct and reflected waves. Resonance mode locations in ACFs are the same as those from the continuous seismic recordings, which could result from either the source or site term, or both. Through inverse Fourier transform, the ACF in the time domain is given by

$$R(t) = (1 + \delta^{2}) \cdot A_{s}(t) + \delta \cdot A_{s}(t - \Delta t) + \delta \cdot A_{s}(t + \Delta t), \tag{S2b}$$

where $A_s(t)$ is the ACF of the direct wave that satisfies $A_s(t) = A_s(-t)$ and $(A_s) = A_s(0)$. The Fourier transform of $A_s(t)$ is given by $\left|\tilde{S}(\omega)\right|^{2}$.

In the analysis of Mars data, the source term, $\left|\tilde{S}(\omega)\right|^{2}$, corresponds to wind-generated lander vibration, thus may include resonance modes at specific frequencies (e.g., 4.1 Hz). These peak frequencies are difficult to infer because they depend on the driving force (i.e., wind activities), the lander's structure (e.g., solar panel) and how the lander is coupled with the ground (Murdoch *et al.* 2017, Morgan *et al.* 2018). The site term, $C_{\delta}(\omega, \Delta t)$, oscillates in the frequency domain producing spectral peaks at $f = (N+0.5)/\Delta t$ and $f = N/\Delta t$, respectively, for negative and positive reflection coefficients δ, where N is an integer.

For vertically incident and reflected SV waves, δ depends on the velocity and density contrasts at the reflection interface (Aki & Richards 1980). In a regular velocity structure on Earth when both velocity and density increase with depth, δ is negative for vertically down-going and reflected up-going SV waves. We notice a negative δ can cause the trough amplitude larger than that of the crest in the ACF, while the ACFs of seismic data on Mars are complicated showing several troughs and crests with similar level of amplitudes (Fig. 3a). On the other hand, the velocity structures on Mars, thus the value of δ, are not very well constrained, but the value of δ doesn't affect the dt/t measurement based on cross-correlation of ACFs.

Here we assume a negative δ. When Δt = 1.36 sec, $C_{\delta}(\omega, \Delta t)$ contains a peak at 3.3 Hz for N = 4, consistent with the observed spectral peak at ~3.3 Hz in the seismic data. Regarding the 4.1 Hz peak, the situation is more complicated. Though the observed 4.1 Hz peak is dominated by the source term (i.e., wind-generated lander vibration at around 4 Hz), it is the result of the convolution between source and site response terms (Equation S2a). When $N = 5$, Equation S2a predicts another site resonance mode at f_l = 4.04 Hz, which is also close to the observed 4.1 Hz peak in the ACF. Therefore, the 4.1 Hz peak of the ACF may also vary with the two-way travel time Δt, no matter whether the lander resonance mode (source term) is time invariant or not. Other spectral peaks from $C_{\delta}(\omega, \Delta t)$ do not stand out in the spectrum of seismic data, probably because the source term doesn't have enough energy in the corresponding frequency band.

It's important to note that performing traditional spectral whitening, by flattening the amplitude of $\widetilde{D}(\omega)$, will distort the reflection signal in time domain, as the amplitude spectrum, $\left|\widetilde{D}(\omega)\right| = \left|\tilde{S}(\omega)\right| \cdot \sqrt{1 + \delta^2 + 2\delta \cdot cos\, cos\, (\omega \Delta t)}$ contains information of the reflection. Therefore, we apply spectral whitening by deconvolving the estimated source term from the ACF, i.e., dividing the ACF spectrum by the approximate source spectrum. The source term is estimated as the running average of the ACF spectrum with a window size of $\Delta f = 1/\Delta t$, assuming that the source spectrum varies smoothly in the window with a size of Δf. In this scenario, the source term only alters the shape of the arrivals in the time domain, and can be suppressed via the deconvolution process.

Monitoring With ACF

Since the ACFs include contributions from source and site terms (Equation S2a), the signal at 1.3 sec in ACFs can be associated with interference of source resonance modes and/or interference of direct and reflected waves (section Monitoring Subsurface Structures Using ACFs). We acknowledge that the active source, i.e. wind-generated lander vibration, is sensitive to fluctuations in temperature and can vary with time (e.g., Murdoch *et al.* 2017, Morgan *et al.* 2018). Here we demonstrate by analytical derivation that the *dt/t* measured from ACFs is not biased by variations of the source spectrum if the 1.3 sec signal in ACF results from interference of direct and reflected waves.

Let $R_{t0}(t)$ and $R_{t1}(t)$ denote ACFs of two seismic recordings with different source wavelets, $S_0(t)$ and $S_1(t)$, and two-way travel times, Δt_0 and Δt_1. The corresponding Fourier transforms are $\tilde{R}_{t0}(\omega)$ and $\tilde{R}_{t1}(\omega)$. Following Equation (S2b), the cross-correlation $cc(t)$ of $R_{t0}(t)$ and $R_{t1}(t)$ at the positive time lag, i.e. $\delta \cdot A_{s0}(t - \Delta t_0)$ and $\delta \cdot A_{s1}(t - \Delta t_1)$, is given by

$$\widetilde{cc}(\omega) = \left|\tilde{S}_0(\omega)\right|^2 \cdot \left|\tilde{S}_1(\omega)\right|^2 \cdot \delta^2 \cdot e^{i\omega(\Delta t_0 - \Delta t_1)}, \tag{S3a}$$

in the frequency domain, and,

$$cc(t) = \delta^2 \cdot A_{cc}\big(t - (\Delta t_0 - \Delta t_1)\big), \tag{S3b}$$

in the time domain, where $A_{cc}(t)$ is the ACF of the signal with the Fourier transform $\left|\tilde{S}_0(\omega)\right|^2 \cdot \left|\tilde{S}_1(\omega)\right|^2$. Since $A_{cc}(t) = A_{cc}(-t)$ and has the maximum value at $t = 0$, $cc(t)$ reaches the maximum at $\Delta t_0 - \Delta t_1$. This suggests that changes in the source term only alter the shape of the correlation function and do not introduce bias into the two-way travel time change estimated via cross correlation.

In Fig. S4, we demonstrate, based on a synthetic test, that a 30% shift in the peak frequency of the source spectrum does not affect our estimation of Δt variation. For the simulation, we use two Ricker wavelets with dominant frequencies of 4.5 Hz and 3 Hz sampled at 100 Hz, respectively, as the direct wave, representing >30% peak frequency change in the source spectrum. We set the reflection coefficient δ = -0.25, and generate seismic recordings D_0 (4.5 Hz) and D_1 (3 Hz) with Δt_0 = 1.3 sec and Δt_1 = 1.365 sec, respectively (Fig. S4a). This suggests a 5% travel time increase. We add random noise to D_0 and D_1 with a signal-to-noise ratio of 4 in the frequency domain. Fig. S4(b) shows the ACFs of D_0 and D_1, and the tapering window that isolates the reflection signal, i.e. the window for cross-correlation. The cross-correlation function of the tapered ACFs is illustrated in Fig. S4(c), showing a maximum value at dt = -0.06 sec. The estimated travel time variation, 0.06 sec, deviates from the true value, 0.065 sec, because the data resolution is 0.01 sec. The maximum cross-correlation coefficient is a bit low (~0.5), due to the added noise and the dramatic variation in the peak frequency of the source spectrum. The result suggests that the significant change (> 30%) in peak frequency of the source spectrum yields no effect on the Δt variation estimated via cross-correlation of the tapered ACF.

Comparison Of The On-deck And On-ground Data

In section Monitoring Subsurface Structures Using ACFs, we propose two hypotheses, interference of source resonance modes and interference of seismic waves in subsurface structure, both of which are compatible with our observations from on-ground data. Here we compare the on-deck and on-ground data, in an effort to distinguish between the two hypotheses.

Fig. S5 shows the EW-component spectrogram, ACFs and H/V ratios for the on-deck data (sols 10, 16, 20, 21). Similar to the on-ground data, we observe spectral peaks at ~3.3, ~4.1, ~6.8, ~8.5 and ~9.8 Hz, and variations in the ACFs. However, we observe differences between the on-ground and on-deck H/V ratios (Fig. S6), where the on-deck H/V ratios show a peak at ~4.1 Hz and a trough at ~3.3 Hz, while the on-ground H/V ratios show peaks at 3.3 Hz and 4.1 Hz.

The similar on-ground and on-deck spectral peak locations and ACFs may indicate they are all lander resonance modes, consistent with the first hypothesis. However, we note the on-deck recording is a convolution of the ground motion and lander response, and the sensor is capable of recording ground motions on the deck. Indeed, the significant difference between the on-ground and on-deck H/V ratios implies footprints of underground signals. Without ruling out the first hypothesis, we focus on demonstrating that the *dt* measurement (section *dt* Measurements) and spectral peak properties at 3.3 and 4.1 Hz (section Properties Of Spectral Peaks at ~3.3 Hz) are compatible with the second hypothesis.

dt Measurements

Since the seismometer only operated during the afternoon and early evenings while on the deck, we focus on the temporal change of the absolute two-way travel time (*dt*) rather than *dt/t*, as the reference two-way travel time *t* is likely different for the on-deck and on-ground data. We compare *dt* curves in Fig. S7, and demonstrate in the following that the observations are compatible with wave resonances in the subsurface structure.

In the two horizontal components, the on-deck *dt* measurements are similar to, but slightly smaller after 8 pm than, those on the ground (Figs S7a-b). This implies the on-deck recording may contain reflected waves, generating the signal at ~1.3 sec in ACF with similar variations. However, the signals are modulated by the lander when the seismometer operated on the deck, i.e. convolved with the lander response which depends on the coupling of the lander's feet with the ground, resulting in the deviation of *dt* measurements from the on-ground data.

In the vertical component, the on-deck *dt* measurements are almost the same as those on the ground (Fig. S7c). The summation of direct and reflected *S*-waves with dominant frequencies of 4.1 Hz generates ground motion resonance at 3.3 Hz in the horizontal directions. This *S*-wave ground motion is then coupled with the lander's foot (i.e. tripod), and transferred to the vertical direction through the lander's response, which preferentially amplifies the vertical ground motion relative to the horizontal (section Properties Of Spectral Peaks at ~3.3 Hz). The lander-transferred vertical motion is either directly recorded by the seismometer on the deck, or transmitted to the subsurface and then recorded by the seismometer on the ground. As a result, the recordings on the deck and ground in the vertical direction are similar in terms of the *dt* measurements (Fig. S7c).

Properties Of Spectral Peaks At ~3.3 Hz

Distinguishing the two hypotheses is equivalent to analyzing the origin of the ~1.3 sec signal or the 3.3 Hz resonance mode in ACFs (section Monitoring Subsurface Structures Using ACFs). Here we analyze the spectral peak properties at 3.3 Hz, from the on-deck and on-ground (sol 98) data. We emphasize again that it's impossible to exclude the first hypothesis due to the complicated structure of the lander and its highly variable vibration patterns. Thus we illustrate that the spectral peak properties at ~3.3 Hz also fit well with the *S*-wave resonance in subsurface structure, based on (1) amplitude ratio between the ~4.1 and ~3.3 Hz resonance modes, $R = A_{4.1Hz}/A_{3.3Hz}$ (Figs S8-S9), and (2) the H/V ratios (Fig. S6).

Since the on-ground sensor is almost co-located with the lander, we expect similar behavior of different lander resonance modes when the seismometer was moved from the deck to the ground. Therefore, assuming the ~3.3 Hz spectral peak, similar to that at ~4.1 Hz, is associated with lander resonance, the *R* value and its correlation with the wind speed are expected to be similar for on-deck and on-ground recordings, and H/V ratios at 3.3 Hz and 4.1 Hz should exhibit similar variations when comparing on-ground and on-deck data.

However, our observations show the opposite. The on-deck *R* value is ~7-10 times larger than the on-ground value at horizontal components, but only ~1/2 of the on-ground *R* value at the vertical component (Fig. S8). Also, the *R* value slightly increases with the wind speed on the deck while remains almost constant for the on-ground data (Fig. S9). In addition, the H/V ratios show peaks at ~4.1 Hz for both the on-deck and on-ground data, whereas at 3.3 Hz contain a significant trough on the deck, but a peak on the ground (Fig. S6).

The deviation of the observation from our expectation could result from the complicated vibration pattern of the lander, thus we do not rule out the contribution from lander vibrations. Instead, we show that these observations are also compatible with the case when the 3.3 Hz resonance mode results from the interference of direct and reflected *S* waves. We note that the on-deck sensor is capable of recording subsurface reflections (Panning & Kedar 2019), and that the lander response preferentially amplifies the vertical motion. First, the 3.3 Hz spectral peak is observed both on the deck and ground, and is compatible with the resonance frequency of a low-impedance layer with a 1.3 sec *S*-wave two-way travel time (section Properties Of ACF With An Active Source). Second, the on-deck *R* values are expected to be larger in the horizontal and smaller in the vertical when compared with the on-ground values, considering the reflected waves are relatively suppressed in the horizontal direction through the lander-ground coupling. These are consistent with our observation in Fig. S8. The amplification of vertical motion on the deck is also compatible with the significant trough in the on-deck H/V ratios at 3.3 Hz. Without the lander-ground coupling issue after the sensor was deployed on the ground, the H/V ratios at 3.3 Hz show a peak, implying amplification of horizontal motions by the subsurface structure.

In summary, the resonance mode at ~3.3 Hz may be related to complicated lander vibration resonance mode, and/or interference of direct and reflected *S* waves. Therefore, we cannot distinguish the two hypotheses, and conclude our observations are most likely the result of a combination of both.

Thermoelastic Strain

The thermoelastic strain in elastic half-space induced by a traveling or stationary temperature wavefield at the surface (Berger 1975) can be expressed as

$$\varepsilon_{xx}(x,y,t) = \left(\frac{1+\sigma}{1-\sigma}\right)\frac{k}{\gamma}\cdot\left\{[2(1-\sigma)-ky]e^{-ky} - \frac{k}{\gamma}e^{-\gamma y}\right\}\beta T_0 e^{i(\omega t+kx)} \quad \text{(S4a)}$$

$$\varepsilon_{yy}(x,y,t) = \left(\frac{1+\sigma}{1-\sigma}\right)\cdot\left\{-\frac{k}{\gamma}(2\sigma-ky)e^{-ky} + e^{-\gamma y}\right\}\beta T_0 e^{i(\omega t+kx)} \quad \text{(S4b)}$$

where x represents the horizontal coordinates, y is the depth and ω is the angular frequency. Here σ is the Poisson's ratio, β is the coefficient of linear thermal expansion, κ is the thermal diffusivity of the elastic half-space, and $\gamma \cong (1+i)(\omega/2\kappa)^{1/2}$ considering $\kappa \ll \omega/k^2$. T_0 and $k = 2\pi/\lambda$ are the amplitude and wavenumber of the temperature field with λ being the wavelength.

The thermoelastic strain at a given depth is a superposition of two terms: (i) 'body force' term associated with the (attenuated and delayed) temperature variation at that depth and (ii) a 'surface traction' term involving transmission of thermoelastic strains generated at a shallower depth that are elastically coupled to that depth. The 'body force' term decreases rapidly with depth, while the 'surface traction' can penetrate to a depth that is on the order of the surface temperature wavelength. If the half-space is covered by unconsolidated material in a (decoupled) surface layer with a thickness of y_b, the thermoelastic strain at the underlying half-space is generated by the delayed and attenuated (by $e^{-\gamma y_b}$) temperature field at the bottom of the surface layer (Ben-Zion & Leary 1986, Ben-Zion & Allam 2013).

The phase delay of thermoelastic strain relative to the temperature field increases with depth, and has a value of $\tau/8$ below the thermal boundary layer (usually less than ~1 m for diurnal variations; Berger 1975, Tsai 2011) with τ being the period of the temperature field. A decoupled surface layer introduced an additional phase delay that equals the time the temperature field travels through the unconsolidated layer (Ben-Zion & Leary 1986). This phase delay of thermoelastic strain is expected to introduce a similar delay to the temporal variations (e.g., dt/t) relative to the surface temperature, but is difficult to measure because of the cumulative contribution from materials at various depths and poorly constrained parameter values on Mars.

Thus, in reasonable ranges of parameter values, we calculate the amplitude of volumetric thermoelastic strain, defined as the summation of horizontal and vertical strains, $\varepsilon_{xx} + \varepsilon_{xx} + \varepsilon_{yy}$, assuming an isotropic deformation in the two horizontal directions. The two parameters κ and β for the elastic half-space are between 10^{-8}-10^{-4} m^2/s and 10^{-5}-10^{-3} °C^{-1}, respectively. The lower bound of κ is set as the value of the near-surface layer on Mars (~10^{-8} m^2/s) estimated by Morgan et al. (2018). The thermal conductivity is ~10^{-2} W m^{-1} K^{-1}, close to the pore-filling CO_2 gas conductivity (Morgan *et al.* 2018). Thus the upper bound of β is on the order of 10^{-3} °C^{-1}. The upper bound of κ and lower bound of β are set as typical values for crystalline rocks under room temperature on Earth (~10^{-6} m^2/s and ~10^{-5} °C^{-1}). In these ranges of parameter values, the amplitude of thermoelastic strain at shallow depth is not sensitive to the wavelength of the temperature field

λ when $\lambda > 500\ m$ (Fig. S10) or the Poisson's ratio σ in the range of 0.1-0.5 (Fig. S11). Thus, we set $\lambda = 15\ km$ and $\sigma = 0.3$ and present the amplitude of thermoelastic strain at different depth ranges in Fig. (S12).

The average thermoelastic strain in the top ~20 m is ~10^{-7}-10^{-5}. In general, intact rocks are less susceptible than soft sediment soils, showing smaller changes in response to the same level of strain. Velocity variations also increase with decreased confining pressure or increased level of fluid content. Laboratory experiments (TenCate *et al.* 2004, Pasqualini *et al.* 2007) show that sandstone and other rocks on Earth begin to suffer material damage under strain levels of about 10^{-7}. Moreover, strain levels in the range 10^{-7}-10^{-6} (associated with the stress level of 10^{1}-10^{2} Pa assuming rigidity of 10^{8} Pa (a value between that for typical crystalline rocks, 10^{9} Pa, and near-surface material on Mars, 10^{7} Pa) can generate velocity changes without causing any material damage under low confining pressure (Nur & Simmons 1969). Studies on soil show more pervasive and large material variations (Beresnev & Wen 1996, Hartzell *et al.* 2004, Bonilla *et al.* 2005) with higher sensitivity to confining pressure, grain size and water content variations (Johnson & Jia 2005, Stokoe *et al.* 2005). In-situ observations on Earth (Qin *et al.* 2020) indicate ~10% average velocity reduction in the top 15-m soil for dynamic strain levels of 10^{-7}-10^{-6}. Considering the extreme environmental conditions, low confining pressure, and weak materials with very low *S*-wave velocities (<100 m/s) at the subsurface of Mars, we expect the thermoelastic strain is capable of generating velocity changes of 10-20% in the top ~20 m, similar to values observed on Earth with autocorrelation analyses of high-frequency seismic waves (e.g., Qin *et al.* 2020, Bonilla & Ben-Zion 2021).

References

Aki, K. & Richards, P.G. (1980) *Quantitative Seismology: Theory and Methods*, W. H. Freeman and Co., San Francisco, California.

Ben-Zion, Y. & Allam, A.A. (2013) Seasonal thermoelastic strain and postseismic effects in Parkfield borehole dilatometers. *Earth Planet. Sci. Lett.*, **379**, 120–126. doi:10.1016/j.epsl.2013.08.024

Ben-Zion, Y. & Leary, P. (1986) Thermoelastic strain in a half-space covered by unconsolidated material. *Bull. Seismol. Soc. Am.*, **76**, 1447–1460.

Beresnev, I.A. & Wen, K.-L. (1996) Nonlinear soil response - a reality? *Bull. - Seismol. Soc. Am.*, **86**(6), 1964-1978.

Berger, J. (1975) A Note on Thermoelastic Strains and Tilts. *J. Geophys. Res.*, **80**, 274–277.

Bonilla, L.F., Archuleta, R.J. & Lavallée, D. (2005) Hysteretic and dilatant behavior of cohesionless soils and their effects on nonlinear site response: Field data observations and modeling. *Bull. Seismol. Soc. Am.*, **95**, 2373–2395. doi:10.1785/0120040128

Bonilla, L.F. & Ben-Zion, Y. (2021) Detailed space–time variations of the seismic response of the shallow crust to small earthquakes from analysis of dense array data. *Geophys. J. Int.*, **225**, 298–310. doi:https://doi.org/10.1093/gji/ggaa544

Hartzell, S., Bonilla, L.F. & Williams, R.A. (2004) Prediction of nonlinear soil effects. *Bull. Seismol. Soc. Am.*, **94**, 1609–1629. doi:10.1785/012003256

Johnson, P.A. & Jia, X. (2005) Nonlinear dynamics, granular media and dynamic earthquake triggering. *Nature*, **437**, 871–874. doi:10.1038/nature04015

Morgan, P., Grott, M., Knapmeyer-Endrun, B., Golombek, M., Delage, P., Lognonné, P., Piqueux, S., *et al*. (2018) A Pre-Landing Assessment of Regolith Properties at the InSight Landing Site. *Space Sci. Rev.*, **214**. doi:10.1007/s11214-018-0537-y

Murdoch, N., Mimoun, D., Garcia, R.F., Rapin, W., Kawamura, T., Lognonné, P., Banfield, D., *et al*. (2017) Evaluating the Wind-Induced Mechanical Noise on the InSight Seismometers. *Space Sci. Rev.*, **211**, 429–455. doi:10.1007/s11214-016-0311-y

Nur, A. & Simmons, G. (1969) The effect of saturation on velocity in low porosity rocks. *Earth Planet. Sci. Lett.*, **7**, 183–193. doi:10.1016/0012-821X(69)90035-1

Panning, M.P. & Kedar, S. (2019) Seismic response of the Mars Curiosity Rover: Implications for future planetary seismology. *Icarus*, **317**, 373–378. doi:10.1016/j.icarus.2018.06.017

Pasqualini, D., Heitmann, K., TenCate, J.A., Habib, S., Higdon, D. & Johnson, P.A. (2007) Nonequilibrium and nonlinear dynamics in Berea and Fontainebleau sandstones: Low-strain regime. *J. Geophys. Res. Solid Earth*, **112**, 1–16. doi:10.1029/2006JB004264

Qin, L., Ben-Zion, Y., Bonilla, L.F. & Steidl, J.H. (2020) Imaging and Monitoring Temporal Changes of Shallow Seismic Velocities at the Garner Valley Near Anza, California, Following the M7.2 2010 El Mayor-Cucapah Earthquake. *J. Geophys. Res. Solid Earth*, **125**, 1–17. doi:10.1029/2019JB018070

Stokoe, K.H., Rathje, E.M. & Axtell, P.J. (2005) Development of an in situ method to measure the nonlinear shear modulus of soil. *Proc. 16th Int. Conf. Soil Mech. Geotech. Eng. Geotechnol. Harmon. with Glob. Environ.*, **2**, 751–754.

TenCate, J.A., Pasqualini, D., Habib, S., Heitmann, K., Higdon, D. & Johnson, P.A. (2004) Nonlinear and nonequilibrium dynamics in geomaterials. *Phys. Rev. Lett.*, **93**, 4–7.

doi:10.1103/PhysRevLett.93.065501

Tsai, V.C. (2011) A model for seasonal changes in GPS positions and seismic wave speeds due to thermoelastic and hydrologic variations. *J. Geophys. Res. Solid Earth*, **116**, 1–9. doi:10.1029/2010JB008156

Supplement Figures

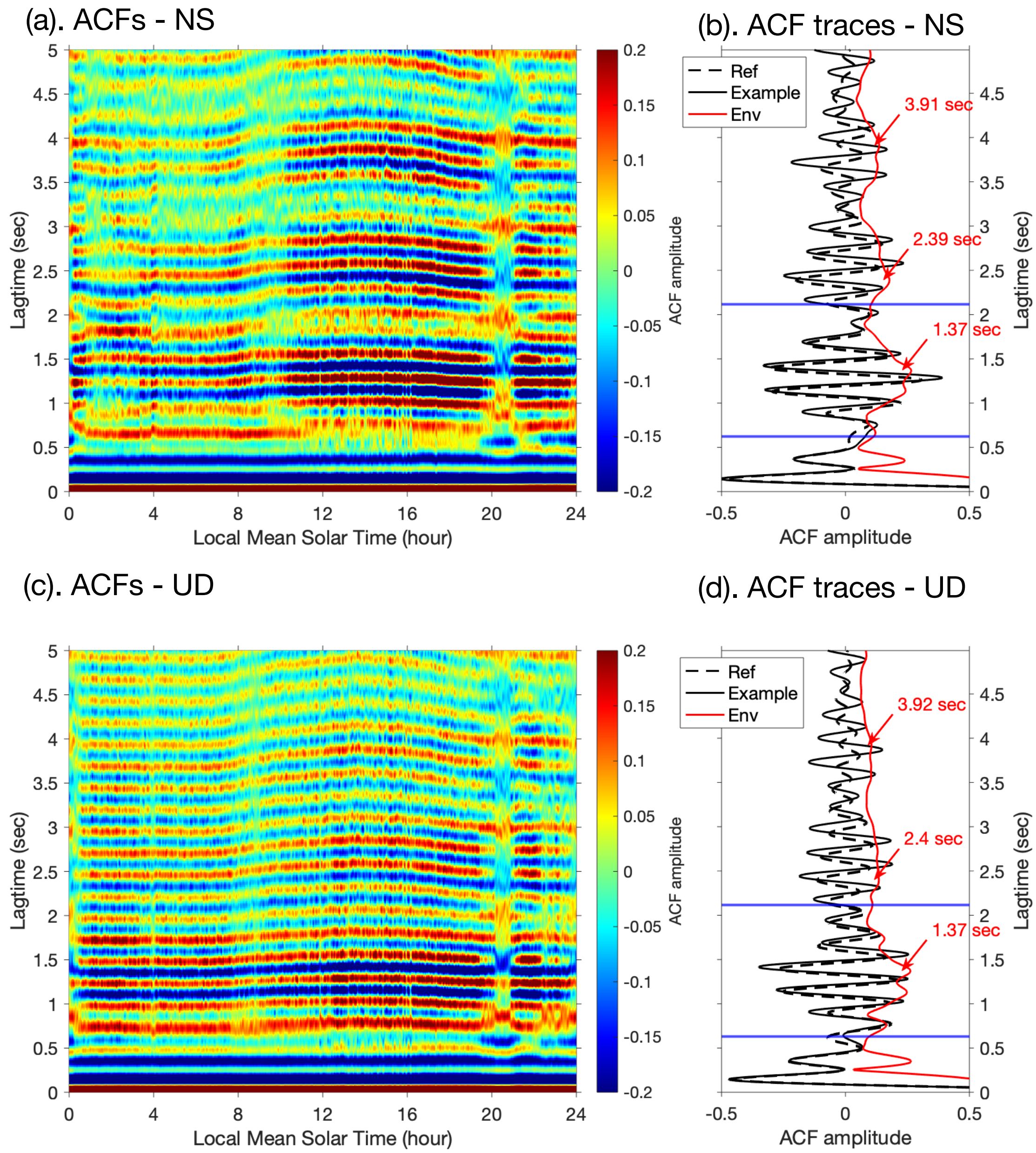

Figure S1. NS (a, b) and vertical (c, d) component ACFs on sol 98. The layouts are similar to Fig. 3.

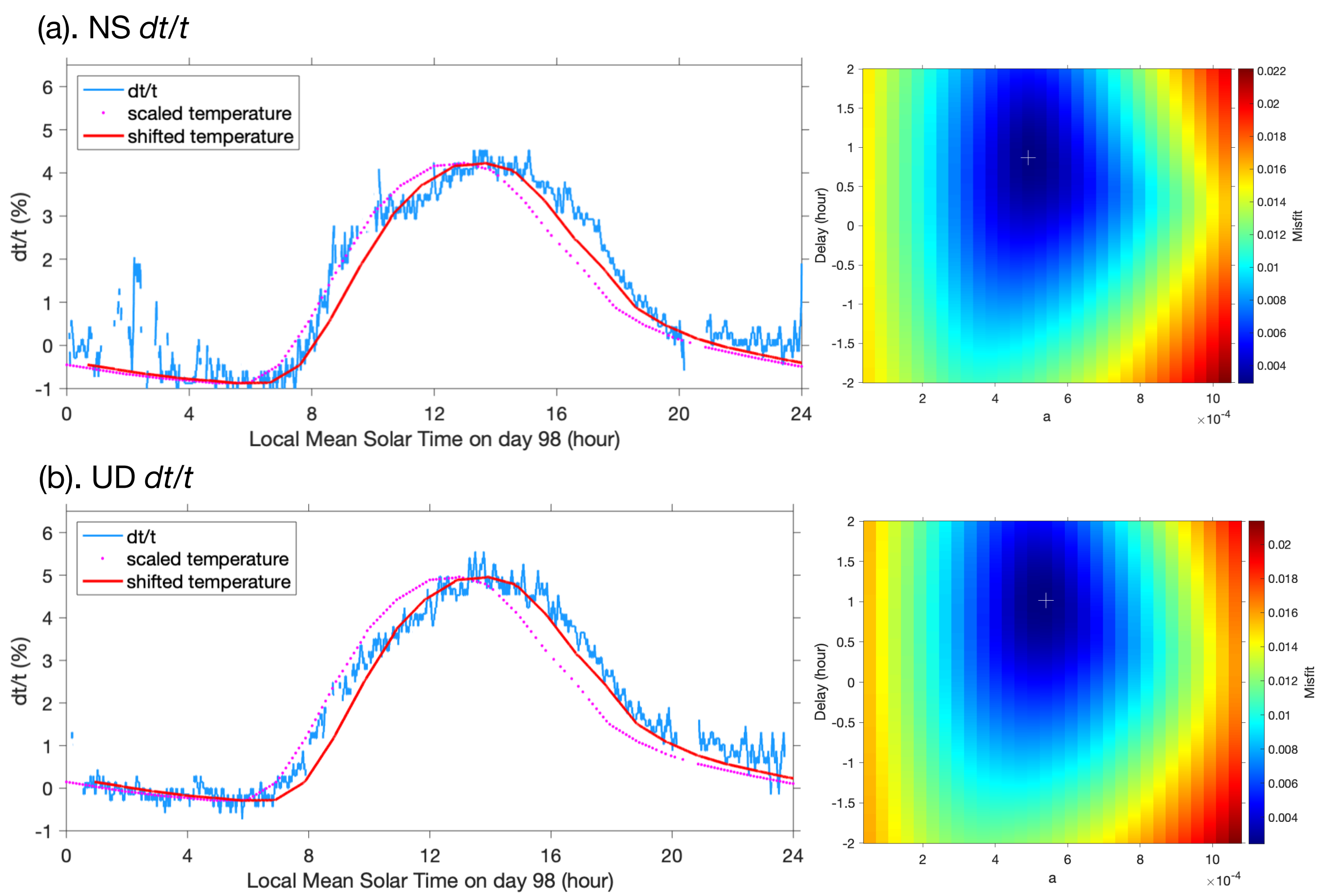

Figure S2. *dt/t* curve fitting results (left panels) and misfit functions (right panels) from NS (a) and vertical (b) component on sol 98. The layout is similar to Fig. 4.

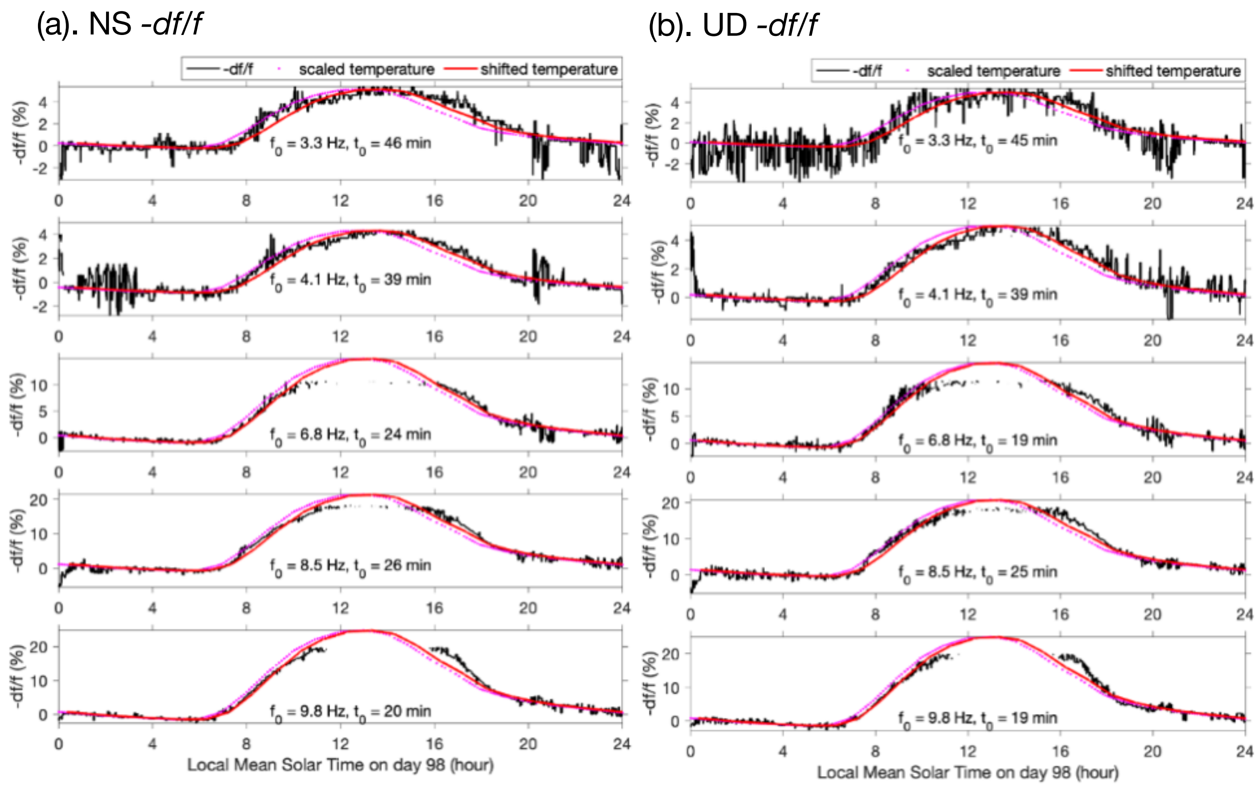

Figure S3. Peak frequency variations *-df/f* (black solid curves) from NS (a) and vertical (b) components at 3.3, 4.1, 6.8, 8.5, and 9.8 Hz, and the best fitting $g(T; a, b, t_0)$ curves (red solid curves). The reference peak frequencies and best fitting time delays are labeled for each panel.

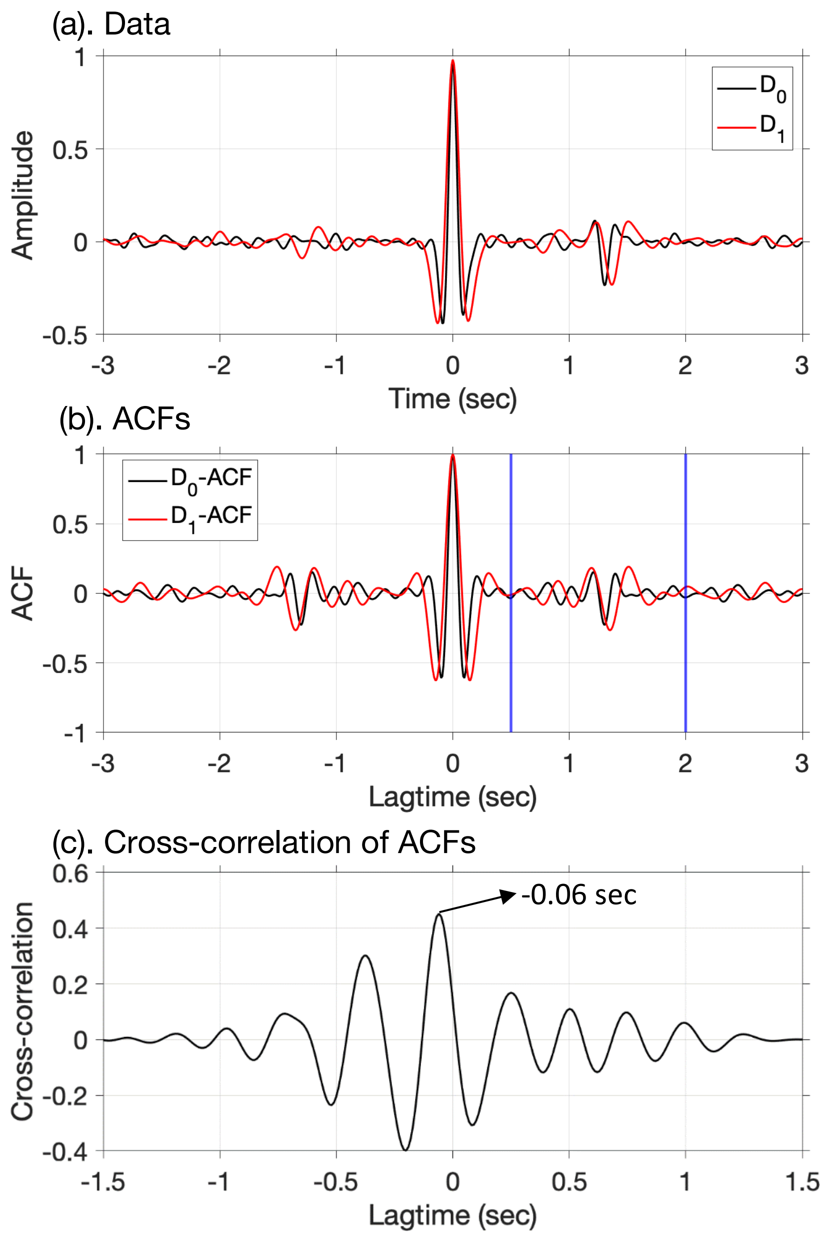

Figure S4. Synthetic test using Ricker wavelets. (a). Two time series with dominant frequencies of 4.5 Hz (D_0) and 3 Hz (D_1), containing reflection phases at 1.3 sec and 1.365 sec, respectively. (b). The normalized ACFs of D_0 (black) and D_1 (red). The blue vertical lines indicate the time window used for cross-correlation. (c) The cross-correlation of the D_0 and D_1 ACFs at 0.5-2 sec, which peaks at -0.06 sec, implying the reflection phase in D_1 is delayed by 0.06 sec with respect to that in D_0.

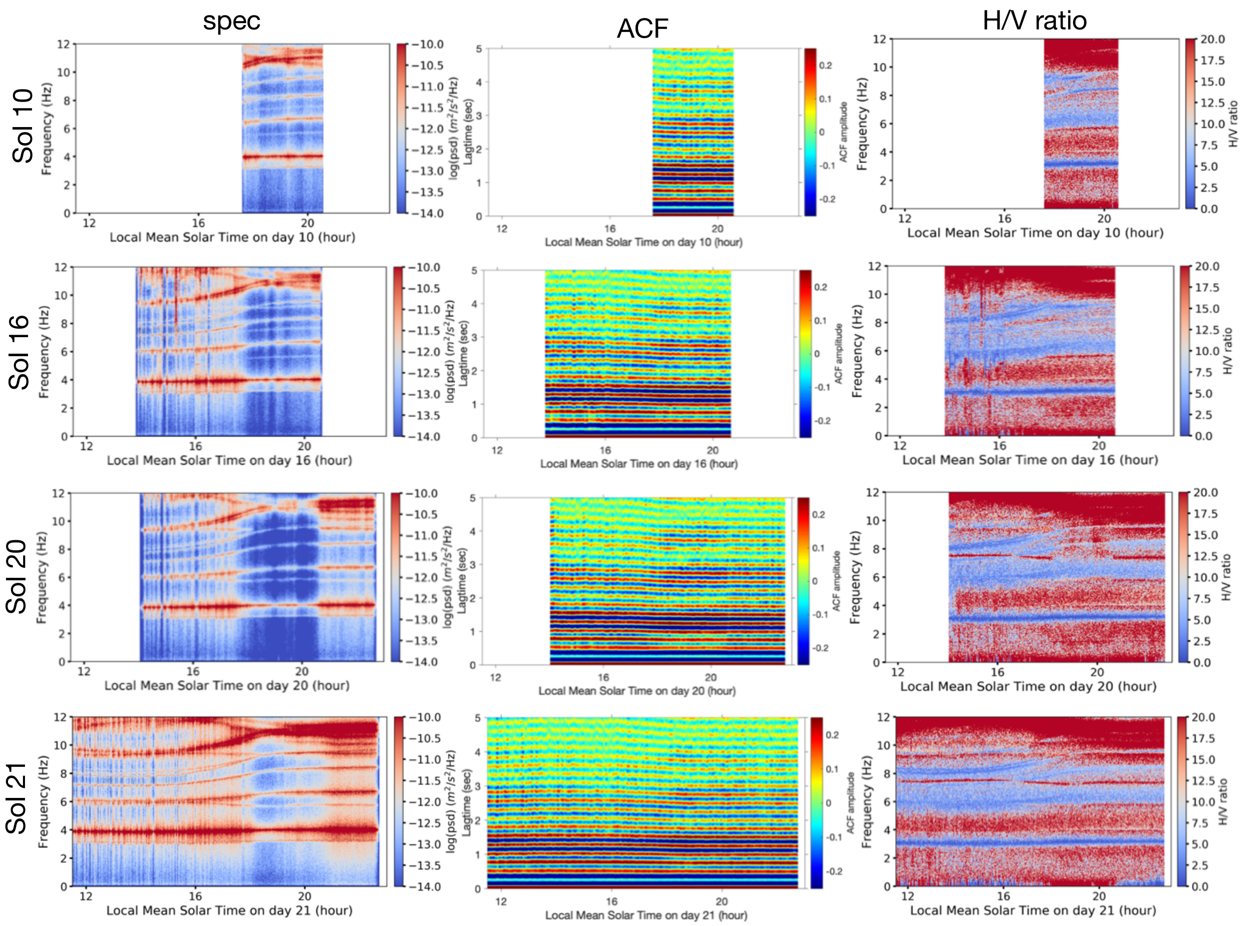

Figure S5. EW-component spectrogram (left column), ACFs (middle column) and H/V ratios (right column) for data on sols 10, 16, 20, 21 when the seismometer operated on the deck.

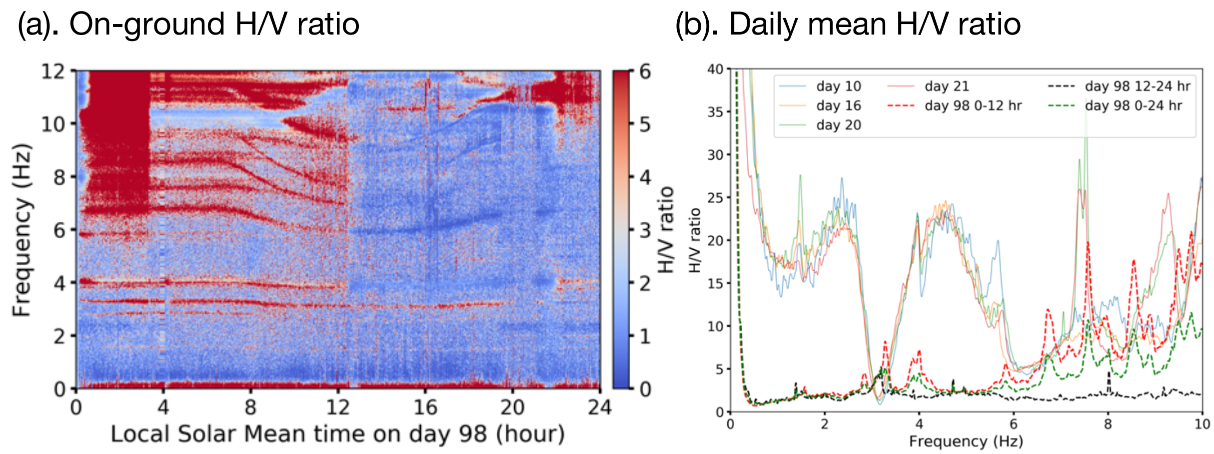

Figure S6. (a) H/V ratios from data on the ground (sol 98). (b) the average H/V ratios between hours 12-23 on the deck (thin colored lines) and average H/V ratios in different time windows on the ground (red dashed line: average from 0-12 hours; black dashed line: average from 12-24 hours; green dashed line: average from the whole day).

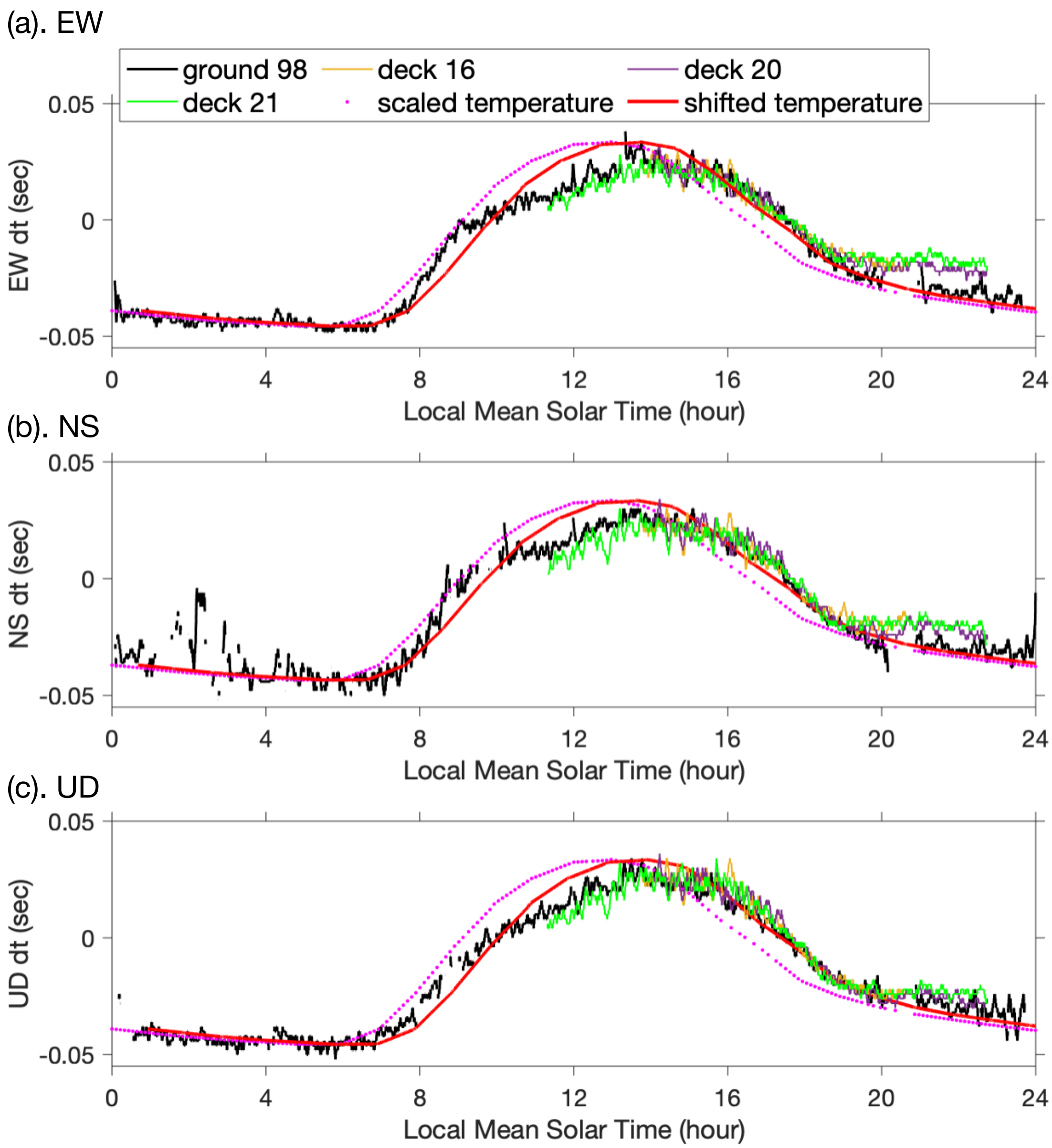

Figure S7. Traveltime variations *dt* from data on the deck (sols 16, 20, 21; colored thin lines) and ground (sol 98; black lines). Linearly scaled temperature (magenta dotted lines) and best fitting curves (red solid lines) are also plotted. The recording on sol 10 is too short (Fig. S5), thus the results are not shown here.

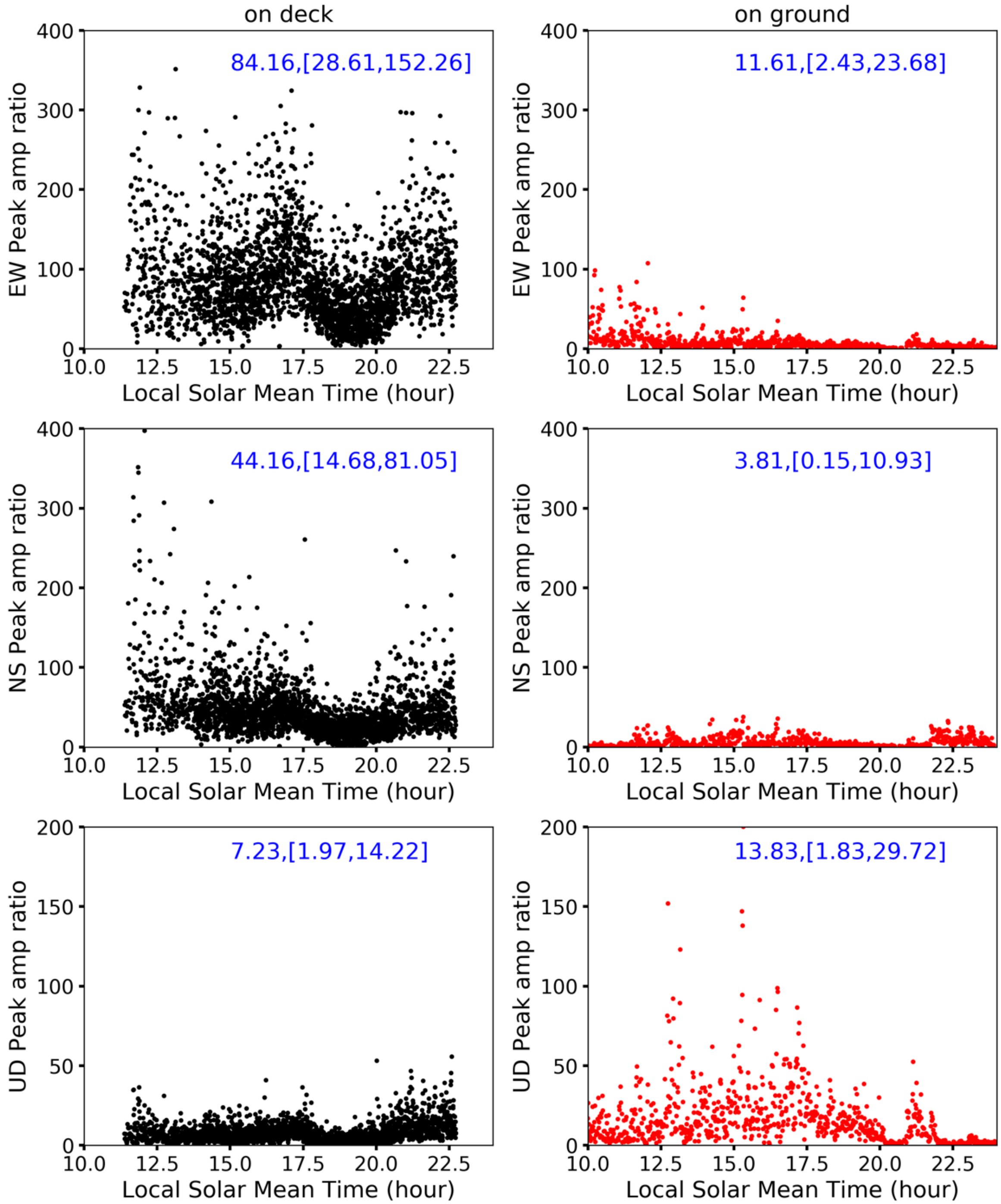

Figure S8. Amplitude ratio between the 4.1 Hz and 3.3 Hz resonance modes in EW (top row), NS (middle row) and vertical (bottom row) components, from data on the deck (left column; black dots; sols 10, 16, 20, 21) and on the ground (right column; red dots; sol 98). The numbers in blue in each subplot represent the mean values and 10 and 90 percentiles.

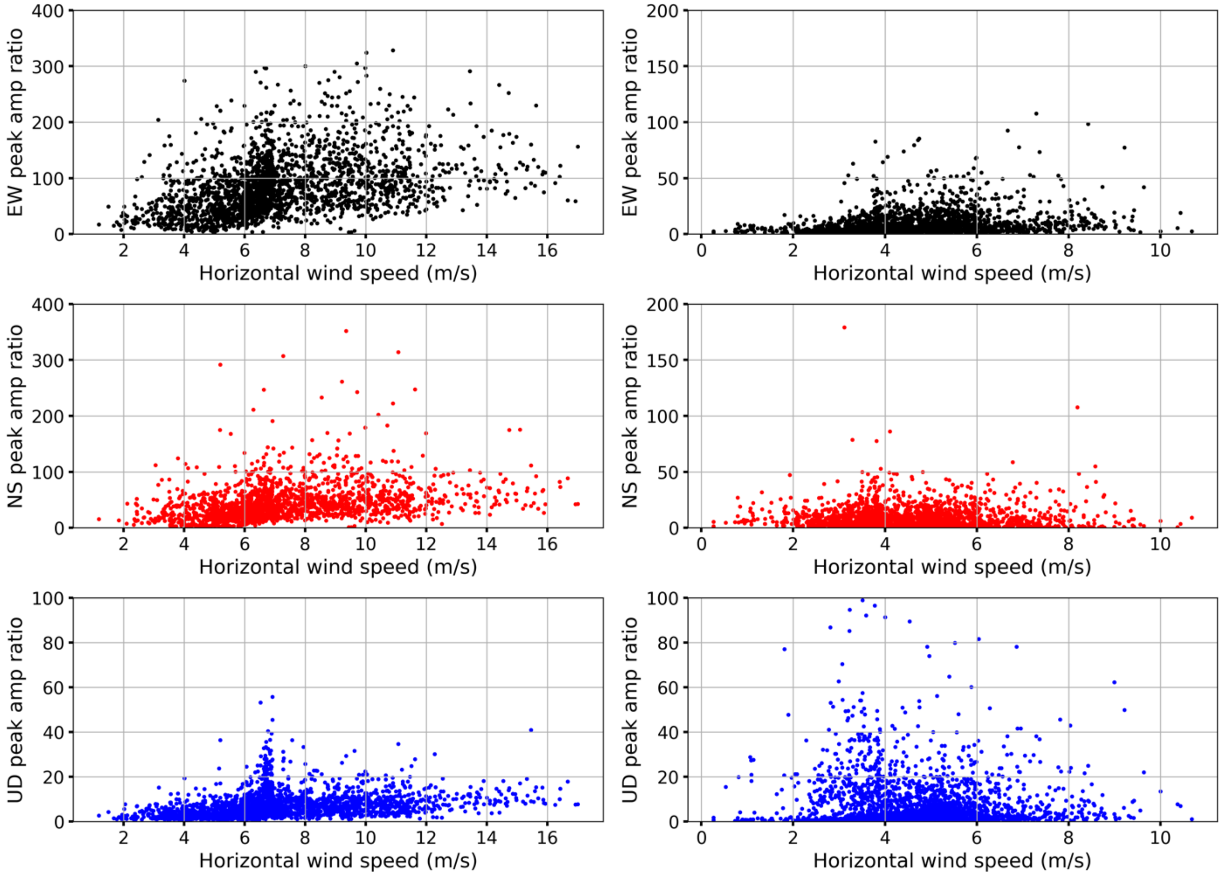

Figure S9. Amplitude ratio between the 4.1 and 3.3 Hz peaks at different horizontal wind speeds for the on-deck (left column) and on-ground data (right column). From top to bottom are results from EW, NS and vertical components, respectively. Please note the different y-axis scales between the left and right columns.

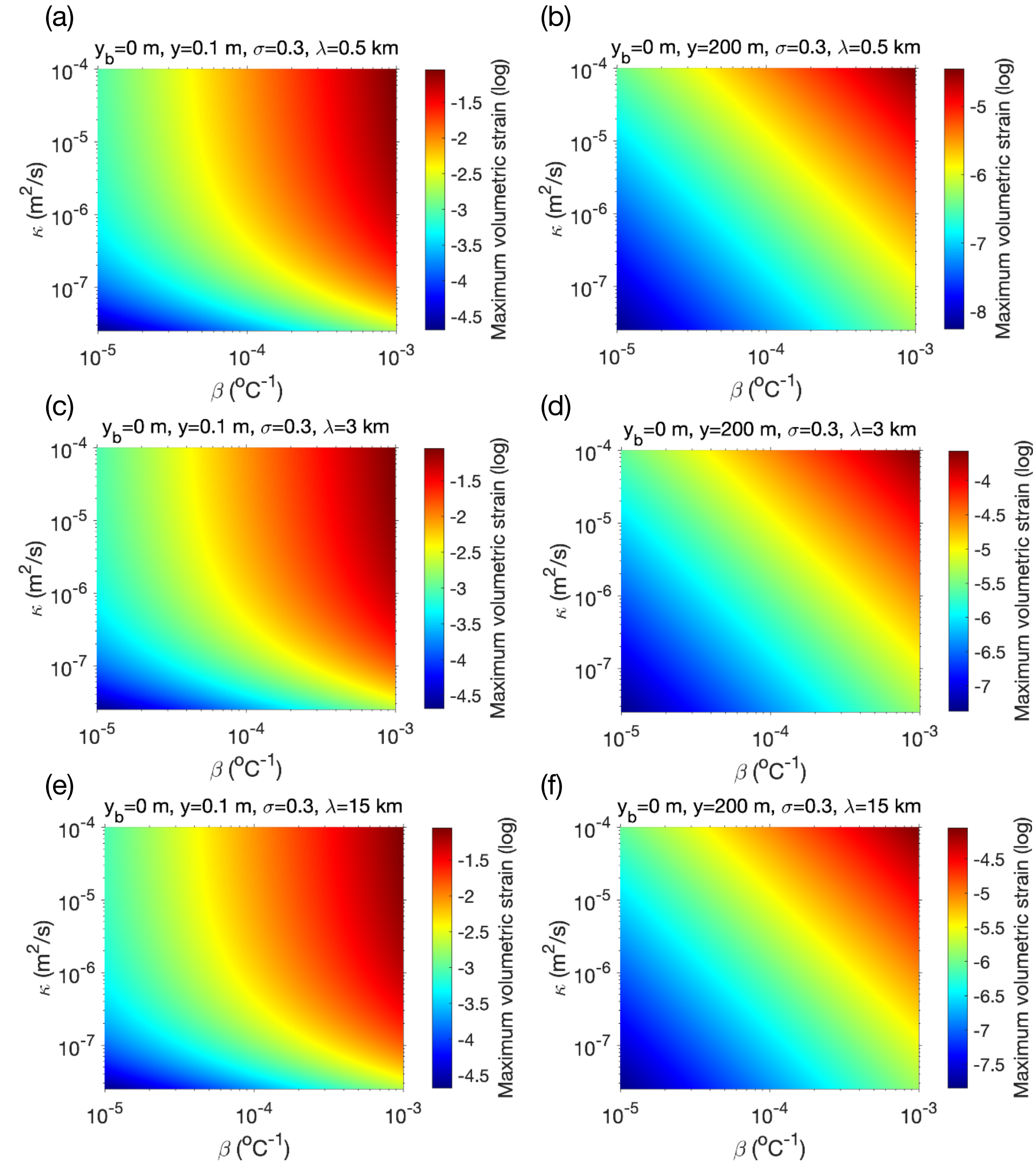

Figure S10. Amplitude of thermoelastic strain calculated at different depths y, 0.1 m (a, c, e) and 200 m (b, d, f) with different wavelengths of temperature field λ 0.5 km (a, b), 3 km (c, d) and 15 (e, f). The Poisson's ratio σ in half-space is set to 0.3. Results are computed for the elastic half space with κ and β ranging from $10^{-8} - 10^{-4}\ m^2/s$ and $10^{-5} - 10^{-3}{}^{\circ}C^{-1}$, respectively.

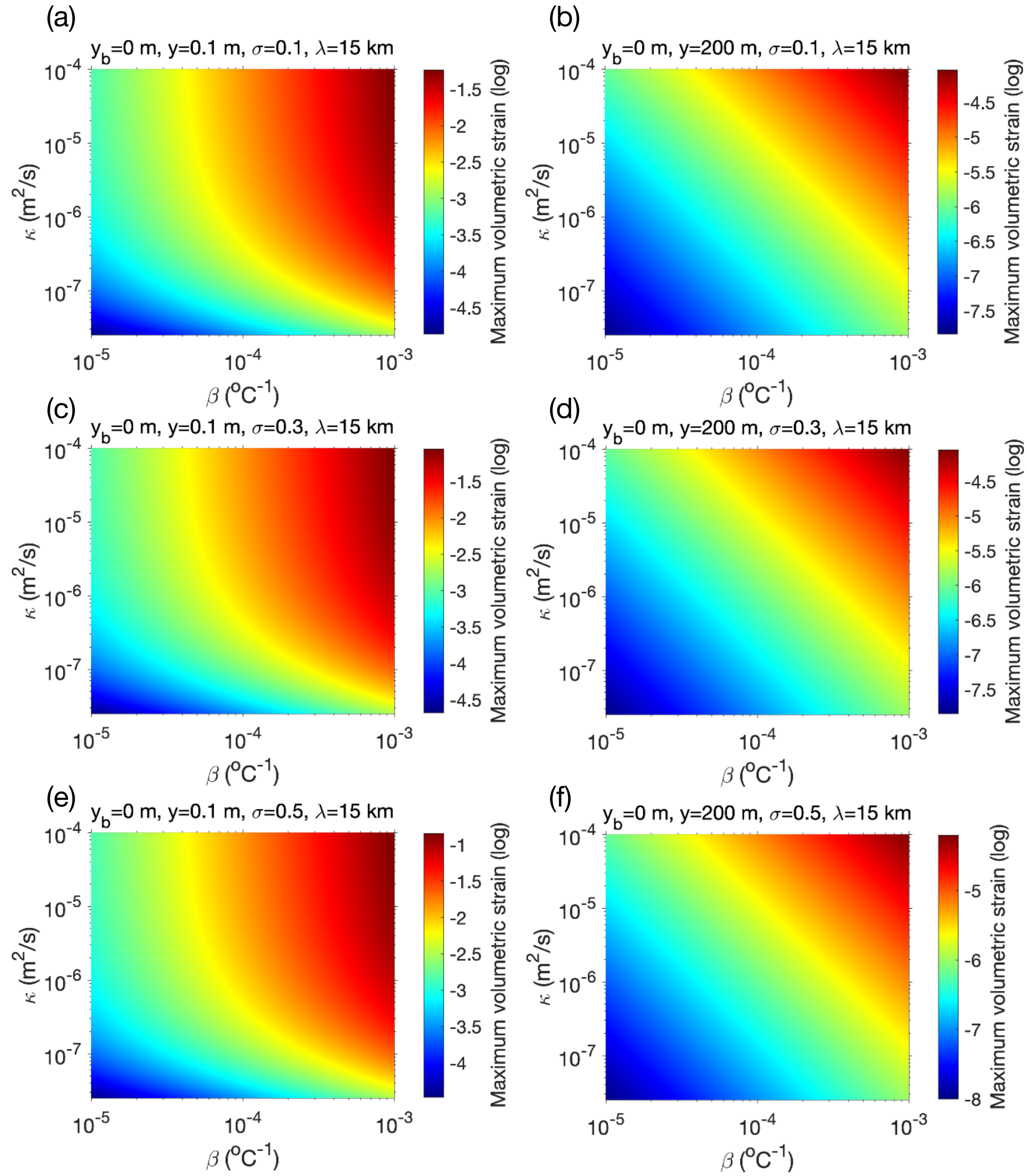

Figure S11. Amplitude of thermoelastic strain calculated at different depths y, 0.1 m (a, c, e) and 200 m (b, d, f) with different half-space Poisson's ratio σ of 0.1 (a, b), 0.3 (c, d) and 0.5 (e, f). The wavelength of temperature field λ is set to 15 km. Results are computed for the elastic half-space with κ and β ranging from $10^{-8} - 10^{-4}\ m^2/s$ and $10^{-5} - 10^{-3\circ}C^{-1}$, respectively.

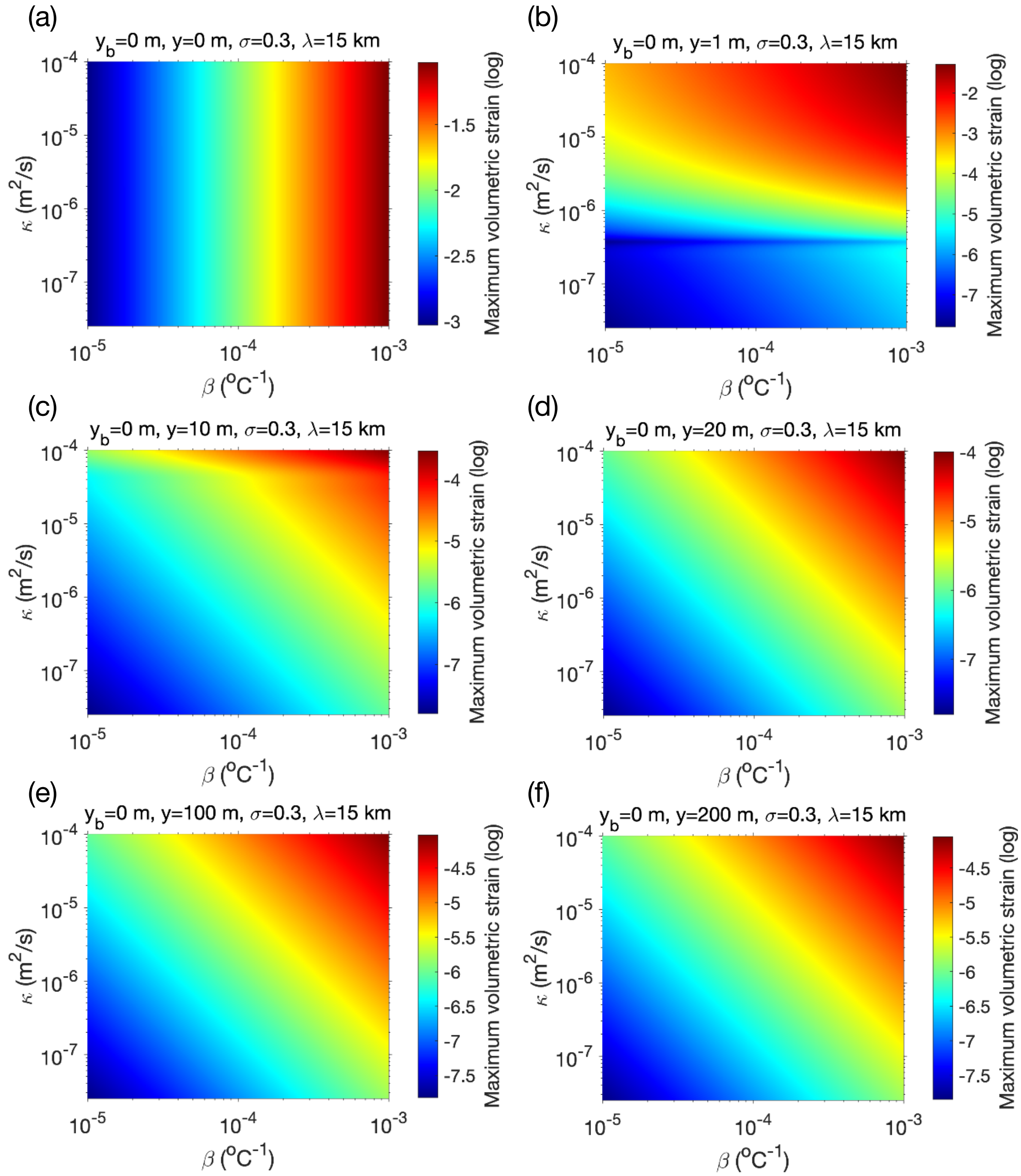

Figure S12. Amplitude of thermoelastic strain calculated at different depths y (0 m, 0.1 m, 1 m, 10 m, 20 m, 100 m, and 200 m). Results are computed for κ and β of the elastic half-space in the ranges 10^{-8}-10^{-4} m^2/s and 10^{-5}-10^{-3} °C^{-1}, respectively. The wavelength of temperature field λ and Poisson's ratio σ are 15 km and 0.3, respectively.

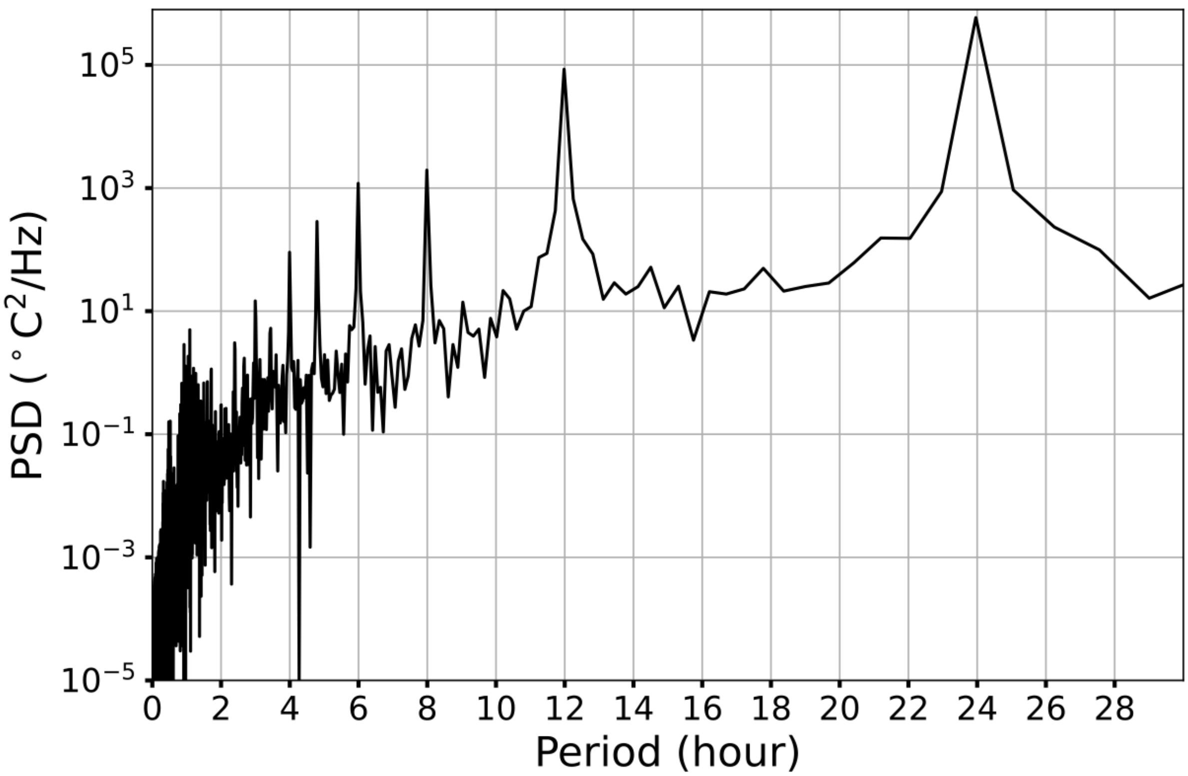

Figure S13. Power spectral density (PSD) of the surface temperature field on Mars.